Monthly Notices
of the
ROYAL ASTRONOMICAL SOCIETY

MNRAS **504,** 1677–1693 (2021)
Advance Access publication 2021 March 24

doi:10.1093/mnras/stab840

The structural evolution of isolated galaxies at low redshift in the IllustrisTNG simulation

Dan Walters [1]★ Joanna Woo,[1,2] Sara L. Ellison [1] and Maan H. Hani [1,3]†

[1]*Department of Physics and Astronomy, University of Victoria, PO Box 1700 STN CSC, Victoria, BC V8W 2Y2, Canada*
[2]*Department of Physics, Simon Fraser University, 8888 University Drive, Burnaby, BC V5A 1S6, Canada*
[3]*Department of Physics and Astronomy, McMaster University, 1280 Main Street West, Hamilton, ON L8S 4M1, Canada*

Accepted 2021 March 16. Received 2021 March 13; in original form 2021 January 5

ABSTRACT

We study the structural evolution of isolated star-forming (SF) galaxies in the IllustrisTNG100-1 hydrodynamical simulation, with a focus on investigating the growth of the central core density within 2 kpc ($\Sigma_{*,2\,\mathrm{kpc}}$) in relation to total stellar mass (M_*) at $z < 0.5$. First, we show that several observational trends in the $\Sigma_{*,2\,\mathrm{kpc}}$–$M_*$ plane are qualitatively reproduced in IllustrisTNG, including the distributions of active galactic nuclei (AGN), SF galaxies, quiescent galaxies, and radial profiles of stellar age, specific star formation rate (sSFR), and metallicity. We find that galaxies with dense cores evolve parallel to the $\Sigma_{*,2\,\mathrm{kpc}}$–$M_*$ relation, while galaxies with diffuse cores evolve along shallower trajectories. We investigate possible drivers of rapid growth in $\Sigma_{*,2\,\mathrm{kpc}}$ compared to M_*. Both the current sSFR gradient and the black hole (BH) accretion rate are indicators of past core growth, but are not predictors of future core growth. Major mergers (although rare in our sample; ∼10 per cent) cause steeper core growth, except for high-mass ($M_* \gtrsim 10^{10}\,\mathrm{M}_\odot$) mergers, which are mostly dry. Disc instabilities, as measured by the fraction of mass with Toomre $Q < 2$, are not predictive of rapid core growth. Instead, rapid core growth results in more stable discs. The cumulative BH feedback history sets the maximum rate of core growth, preventing rapid growth in high-mass galaxies ($\gtrsim 10^{9.5}\,\mathrm{M}_\odot$). For massive galaxies, the total specific angular momentum of accreting gas is the most important predictor of future core growth. Our results suggest that the angular momentum of accreting gas controls the slope, width, and zero-point evolution of the $\Sigma_{*,2\,\mathrm{kpc}}$–$M_*$ relation.

Key words: galaxies: evolution – galaxies: general – galaxies: stellar content – galaxies: structure.

1 INTRODUCTION

The structural evolution of galaxies is an integral part of their overall evolution. The sizes, morphologies, and central stellar mass densities of galaxies correlate with their total stellar masses, star formation activity, and environments (Strateva et al. 2001; Kauffmann et al. 2004; Bell 2008; Wuyts et al. 2011; Mendel et al. 2013; Bluck et al. 2014; Schawinski et al. 2014). The average galaxy size at fixed stellar mass grows with decreasing redshift (van der Wel et al. 2014; Barro et al. 2017) in part due to the growth of individual galaxies (Hopkins et al. 2009; Naab, Johansson & Ostriker 2009; Damjanov et al. 2011; van Dokkum et al. 2014). Furthermore, low star formation activity (quiescence) correlates more strongly with various measures of size/morphology than with any other galaxy property (the 'morphology–quiescence' relation; Woo & Ellison 2019; see also Bell 2008; Bluck et al. 2014; Woo et al. 2015; Teimoorinia, Bluck & Ellison 2016).

The basic physical framework for galaxy growth is mostly understood: galaxies are expected to build up their stellar mass from the inside-out as a consequence of the top-hat spherical collapse model where expanding shells of dark matter turnaround and collapse forming dark matter haloes. The innermost shells collapse first, as a result, the gas with the lowest angular momentum settles into the galaxy earliest, giving rise to negative age gradients (the central regions are the oldest; Fall & Efstathiou 1980; Kepner 1999; van den Bosch 1998, 2001). This inside-out growth of galaxies is confirmed in hydrodynamical simulations (e.g. Roškar et al. 2008; Tacchella et al. 2016; Tissera et al. 2016), and inferred in observations (Nelson et al. 2012; Pérez et al. 2013; Tacchella et al. 2015). The inside-out growth mode can be thought of as the 'default' mode for galaxy growth.

Deviations from the inside-out mode include dramatic events such as high-z 'compaction' that drives gas (and sometimes stars) from the outside-in to the central regions of galaxies. Such events produce a central starburst that significantly increases the central stellar density (or perhaps equivalently, grows the bulge) rapidly (Zolotov et al. 2015). Dissipative inflows of gas can be triggered by galaxy mergers (Barnes & Hernquist 1991; Mihos & Hernquist 1996; Hopkins et al. 2006) or gravitational disc instabilities (Friedli & Benz 1995; Immeli et al. 2004; Bournaud et al. 2011). These inflows build the central density causing steeper density profiles. The steeper density profiles result in smaller effective radii (hence 'compaction'). Although events such as compaction appear to be deviations from the default inside-out growing mode, there are indications that compaction is an important event in the life of most galaxies, occurring primarily around $z \sim 2$ (Lapiner, Dekel & Dubois 2020).

In addition to increasing the central density of a galaxy, compaction events also potentially feed active galactic nuclei (AGNs), which are thought to be necessary for quenching galaxies (e.g.

★ E-mail: danwalters@uvic.ca
† Herschel Fellow.

Cattaneo & Teyssier 2007; Woo et al. 2015; Nelson et al. 2018). The association of AGNs with the growth of the central density is one proposed explanation for the morphology–quiescence relation (Zolotov et al. 2015; Woo & Ellison 2019).

Although compaction was originally envisioned as a high-z phenomenon, Woo & Ellison (2019, hereafter WE19) found evidence at $z < 0.07$ for both the default inside-out growth mode as well as a 'compaction-like' mode. They studied gradients of stellar age and star formation rate (SFR) in the Mapping Nearby Galaxies at the Apache Point Observatory survey (MaNGA; Bundy et al. 2015) and found that while galaxies with low central densities have older centres and lower central specific SFRs (sSFR) than their outskirts, galaxies with higher central densities tend to have relatively younger centres and more centrally concentrated star formation. WE19 interpreted the latter observation as a low-z version of 'compaction' (listing various triggers), but acknowledged other possible interpretations.

Tacchella et al. (2019) studied the morphological evolution of galaxies during quenching in the IllustrisTNG (hereafter TNG) cosmological simulation (Pillepich et al. 2017; Marinacci et al. 2018; Naiman et al. 2018; Nelson et al. 2018, 2019; Springel et al. 2018). Although they point out that the growth of the supermassive black hole (SMBH) is related to the growth of the bulge, they argue that the dominant reason for the morphology–quiescence relation is the early quenching of most of today's quiescent (Q) galaxies, when concentrations were high and spheroids form most efficiently. Yet the analysis of Tacchella et al. (2019) also shows that galaxy concentrations do increase during the transition to quiescence (see their fig. 9), and therefore morphological transformation during quenching cannot be ruled out. It remains unclear whether the increase in central density (or concentration or bulge mass) during quenching is a significant transformation compared to the growth of the stellar mass.

The question of morphological/structural transformation during quenching is not a trivial matter, and requires that we first understand the structural growth of *star-forming* (SF) galaxies. Therefore, the aim of this study is to investigate the growth of the central density in isolated SF galaxies. We investigate the growth of galaxy central density in the IllustrisTNG simulation. We first check that the age and sSFR gradients vary with central density and stellar mass at $z \sim 0$ in the same qualitative way as observed in the real Universe (they do). Then, we investigate the physical mechanisms that give rise to these gradients. In particular, why do galaxies with high central densities have centrally concentrated sSFRs? Are compaction-like processes responsible for their high central densities or were their high central densities established long ago? WE19 argue that compaction-like events will result in steeper evolutionary paths in the $\Sigma_{*,1\,\mathrm{kpc}}$–$M_*$ diagram compared to the inside-out mode of galaxy growth (see also Zolotov et al. 2015; Barro et al. 2017). Does the steepness of these paths correlate with certain galaxy properties that lead to the build-up of the central density? Among these properties, we investigate the role of disc instabilities, the occurance of mergers, black hole (BH) feedback, and the angular momentum of the accreting gas as possible reasons for the build-up of dense cores.

This paper is structured as follows. First, in Section 2 we discuss our methodology. Next, in Section 3 we present our results, including a comparison of TNG with observations, an examination of the evolutionary pathways of TNG subhaloes, and an investigation of possible drivers of core growth. In Section 4, we discuss the implications of our findings. Lastly, we summarize our conclusions in Section 5.

2 METHODS

2.1 Simulation

TNG is a set of large-box, cosmological gravo-magnetohydrodynamical simulations evolved from $z = 127$ to the present (Pillepich et al. 2017; Marinacci et al. 2018; Naiman et al. 2018; Nelson et al. 2018, 2019; Springel et al. 2018). TNG assumes a ΛCDM cosmology with parameters consistent with the Planck 2015 results (Ade et al. 2016). The physical model employed in TNG includes a variety of subgrid physics, including stochastic star formation, supernova feedback, stellar evolution and winds, and supermassive BH seeding, growth, and feedback (including both low- and high-accretion rate modes). The TNG model is calibrated to reproduce certain galaxy statistical properties, including the size–mass relation, the cosmic SFR density, and the BH–stellar mass relation (Pillepich et al. 2017). Haloes and subhaloes (galaxies) are identified using friends-of-friends (FOF) and SUBFIND algorithms, respectively (Springel et al. 2001). Note that we use the terms subhalo and galaxy interchangeably.

AGNs in TNG are modelled to inject energy into the surrounding gas in either a low- or high-accretion rate mode (Weinberger et al. 2017). The low-accretion rate mode injects kinetic energy, while the high-accretion rate mode injects thermal energy. The mode each BH is in depends primarily on the accretion rate and the mass of the BH, where the scaling relation favours the thermal mode for low-mass ($\lesssim 10^{8.2}\,\mathrm{M}_\odot$) BHs, and the kinetic mode for high-mass BHs (Terrazas et al. 2020). The kinetic mode couples much more efficiently with the surrounding gas, and lengthens the cooling time of the circumgalactic medium (Zinger et al. 2020). In either case, the energy released is directly proportional to the accretion rate.

In this paper, we use the TNG100-1 simulation that is the highest resolution volume that is currently publicly available. TNG100-1 simulates a cosmological cube with a comoving side length of 100 cMpc. In TNG100-1, there are 22 554 subhaloes resolved with $M_* > 10^9\,\mathrm{M}_\odot$ at $z = 0$. In order to check the effects of spatial resolution, we also analyse the lower resolution version TNG100-2. This is discussed in Section 4.3.

2.2 Subhalo selection

We limit our analysis to galaxies whose z = 0 descendant is an isolated central galaxy with $M_* > 10^9\ \mathrm{M}_\odot$. We define a central subhalo as isolated if the second most-massive subhalo in the FOF group has a stellar mass <20 per cent of the central's stellar mass, and $<10^9\ \mathrm{M}_\odot$. Lastly, we remove any subhaloes flagged by the TNG collaboration as non-physical.

We further divide our sample into SF, Q, and a third category we dub 'intermediate' galaxies (Fig. 1). In the simulation, subhaloes with SFR below the numerical resolution limit are assigned SFR = 0 (see Donnari et al. 2019 for a discussion). Q subhaloes have unresolved SFRs (i.e. SFR = 0), while SF subhaloes have $\mathrm{sSFR} > 10^{-11}\ \mathrm{yr}^{-1}$ that corresponds to the commonly used observational limit of SF versus Q galaxies. Observationally, the non-zero sSFR values reported for Q galaxies are actually upper limits. We define subhaloes with $0\ \mathrm{yr}^{-1} < \mathrm{sSFR} \leq 10^{-11}\ \mathrm{yr}^{-1}$ as 'intermediate' galaxies.

Our goal is to investigate the 'low-redshift' evolution in order to compare our results with Woo & Ellison (2019), therefore we investigate TNG galaxies at $z < 0.5$ (∼5 Gyr in lookback time) that gives us sufficient history to determine galaxy evolutionary trends. The snapshot time resolution of our sample is ∼113–236 Myr.

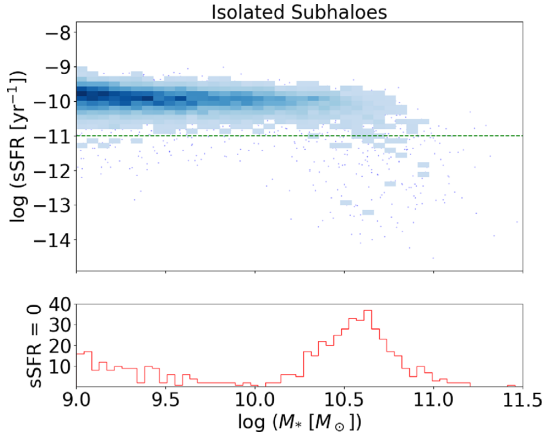

Figure 1. Top panel: The sSFR–M_* relation in TNG at $z = 0$. The horizontal dashed line shows the limiting sSFR required for subhaloes to be defined as SF. Below this dashed line, subhaloes are classified as 'intermediate' if the $0\ \mathrm{yr}^{-1} < \mathrm{sSFR} \leq 10^{-11}\ \mathrm{yr}^{-1}$ and quenched if $\mathrm{sSFR} = 0$. Lower panel: Distribution stellar mass in the subhaloes with unresolved SFR (i.e. quenched).

2.3 The central stellar mass surface density $\Sigma_{*,2\,\mathrm{kpc}}$

Our goal is to investigate the coevolution of central stellar density and stellar mass. The central density is commonly measured as the stellar mass surface density within a fixed radius, e.g. 1 kpc ($\Sigma_{*,1\,\mathrm{kpc}}$) or 2 kpc ($\Sigma_{*,2\,\mathrm{kpc}}$), or generally $\Sigma_{*,N\,\mathrm{kpc}}$, to represent the 'compactness' of a galaxy's core (Cheung et al. 2012; Fang et al. 2013; Woo et al. 2015, 2017; Mosleh et al. 2017; Tacchella et al. 2017; Woo & Ellison 2019). Simulations show that fixed-radius surface densities remain remarkably constant when star formation ceases in the core, whereas densities within a scale radius (e.g. the half-mass radius) experience large fluctuations due also to changes in the galaxy's outskirts (Zolotov et al. 2015; Wellons et al. 2016; Barro et al. 2017). In the absence of new star formation, $\Sigma_{*,N\,\mathrm{kpc}}$ decreases slightly due to stellar mass-loss as the population ages, but overall, the primary changes to $\Sigma_{*,N\,\mathrm{kpc}}$ are driven by dissipative gas processes such as compaction, making $\Sigma_{*,N\,\mathrm{kpc}}$ a good tracer of such processes. In any case, for undisturbed SF galaxies, $\Sigma_{*,N\,\mathrm{kpc}}$ tightly correlates with the effective radius (Chen et al. 2020; Luo et al. 2020).

In this work, we use 2 kpc to quantify the central density ($\Sigma_{*,2\,\mathrm{kpc}}$), so as to sit comfortably above the resolution of TNG (gravitational softening length 0.74 kpc). The surface density within a fixed radius is subject to projection effects, largely ignored in observational data. To investigate these effects, we measure $\Sigma_{*,2\,\mathrm{kpc}}$ for TNG galaxies using three methods. First, we project all subhalo star particles on to a random plane, then sum the mass of particles within the desired radius of the subhalo centre. Second, we project the star particles on to a plane perpendicular to the subhalo stellar component angular momentum vector before summing, giving a 'face-on' measure of $\Sigma_{*,2\,\mathrm{kpc}}$. Third, we sum the mass of star particles within the 3D desired radius from the subhalo centre (i.e. without projecting). In all cases, we divide by the surface area, πr^2. We note that in the case of the 3D value, the calculated $\Sigma_{*,2\,\mathrm{kpc}}$ is not a true surface density. However, it is useful for investigating whether any 'observed' compaction-like behaviour is biased by projection effects rather than a true core density increase. We find that projection effects tend to artificially increase $\Sigma_{*,2\,\mathrm{kpc}}$ by ∼0.2 dex for spheroids and ∼0.3 dex for disc galaxies compared to the true 3D mass within 1 kpc divided by πr^2. Since these effects are independent of mass, the overall effect is a vertical shift in the $\Sigma_{*,2\,\mathrm{kpc}}$–$M_*$ relation that is slightly different between Q and SF galaxies. When examining subhalo histories, we use the face-on projected value to remove any possible effects of projection should the subhalo's angular momentum direction change over time. When comparing to observations, we use the random projection to give as close a comparison as possible.

Although $\Sigma_{*,1\,\mathrm{kpc}}$ pushes the resolution of TNG100-1, we repeated our analysis using $\Sigma_{*,1\,\mathrm{kpc}}$ and find essentially the same trends as with $\Sigma_{*,2\,\mathrm{kpc}}$.

2.4 Calculation of radial gradients

In order to verify that TNG reproduces observed gradients as a function of $\Sigma_{*,2\,\mathrm{kpc}}$ and M_* (WE19), we calculate stellar age, sSFR, and gas phase metallicity gradients for all TNG subhaloes. We compute 'two-point' radial gradients using quantities measured within the stellar half-mass radius (R_e) and $2R_\mathrm{e}$. While this is not strictly analogous to the method used by WE19, our method provides a qualitative comparison with WE19. As we shall see in Section 3, the two-point radial gradient in stellar age and sSFR computed for the TNG galaxy sample are in qualitative agreement with the WE19 observational results.

In the case of stellar age, we calculate the mass-weighted average age of all star particles within the area of interest as follows:

$$\nabla_r \log \mathrm{age} = \frac{\log \frac{\sum_{\mathrm{out}}(m_*)(\mathrm{age}_*)}{\sum_{\mathrm{out}} m_*} - \log \frac{\sum_{\mathrm{in}}(m_*)(\mathrm{age}_*)}{\sum_{\mathrm{in}} m_*}}{\log(1.5R_\mathrm{e}) - \log(0.5R_\mathrm{e})}. \quad (1)$$

For sSFR and gas phase metallicity, we calculate gradients as

$$\nabla_r \mathrm{sSFR} = \frac{\log \frac{\sum_{\mathrm{out}} \mathrm{SFR}}{\sum_{\mathrm{out}} m_*} - \log \frac{\sum_{\mathrm{in}} \mathrm{SFR}}{\sum_{\mathrm{in}} m_*}}{\log(1.5R_\mathrm{e}) - \log(0.5R_\mathrm{e})}, \quad (2)$$

$$\nabla_r \log \mathrm{O/H} = \frac{\log \frac{\sum_{\mathrm{out}} m_{\mathrm{gas,O}}}{\sum_{\mathrm{out}} m_{\mathrm{gas,H}}} - \log \frac{\sum_{\mathrm{in}} m_{\mathrm{gas,O}}}{\sum_{\mathrm{in}} m_{\mathrm{gas,H}}}}{\log(1.5R_\mathrm{e}) - \log(0.5R_\mathrm{e})}. \quad (3)$$

The subscript 'in' refers to particles within $r < R_\mathrm{e}$ while 'out' refers to particles within $R_\mathrm{e} < r < 2R_\mathrm{e}$.

2.5 Tracking galaxy history

We track subhaloes' histories using the SUBLINK merger trees (Rodriguez-Gomez et al. 2015). For each isolated subhalo selected at $z = 0$, we track the main progenitor branch (MPB) back to $z = 0.5$ (∼5.2 Gyr). We choose $z = 0.5$ as it represents the relatively recent universe, while providing sufficient evolutionary histories for the galaxies within our sample.

We tag each subhalo's history any time a progenitor on its MPB undergoes a major merger. Following Rodriguez-Gomez et al. (2015), we define a major merger as having a mass ratio of at least 1:10 between the subhalo's most massive and next most massive progenitors. To avoid histories that undergo subhalo 'switching', we follow the method used by Genel et al. (2018). Specifically, we exclude from our analysis subhaloes whose MPB experiences a relative mass drop of >0.5 over one snapshot.

2.6 Calculation of Toomre parameter

As part of our analysis, we calculate the Toomre stability parameter (Q) of the gas and stellar disc components of the TNG subhaloes. We roughly follow the method used by Inoue et al. (2016). The Toomre parameter (Q) measures the local stability in response to an

axisymmetric density perturbation for a thin disc (Toomre 1964), and it is given by

$$Q = \frac{\sigma \kappa}{AG\Sigma}, \tag{4}$$

where σ is the velocity dispersion, κ is the epicyclic frequency (a measure of the potential), A is a constant (π for the gas component or 3.36 for the stellar component), G is the gravitational constant, and Σ is the surface density. All values are local values, as is Q. Areas with $Q < Q_{\rm crit}$ indicate local instability. $Q_{\rm crit}$ is classically 1, although discs may be unstable up to $Q \sim 2$ (Elmegreen 2011). Initially, we compute Q separately for the stellar and gaseous disc components, then combine them to create a single Q map for each subhalo.

We smooth all physical values by treating the simulation particles as Gaussian functions with fixed smoothing length. The results presented here use a smoothing length of 0.74 kpc, equivalent to the gravitational softening length for collisionless particles in TNG100-1, and therefore the maximum resolution we can achieve for resolving instabilities. To combine values into our Q maps, we apply a mesh to each subhalo with a fixed number of cells within $2R_{\rm e}$ (i.e. over a box $4R_{\rm e} \times 4R_{\rm e}$). Physical values are calculated at the centre of each mesh point. The results here use a 70×70 mesh. Prior to computing Toomre maps at all snapshots using our fiducial smoothing length and mesh size, we tried varying both for a single snapshot. We find no qualitative difference in single snapshot distribution if we vary the smoothing length as low as 0.37 kpc nor if we vary the mesh to as fine as 140×140 within the same box.

Our first step in creating maps of Q for each galaxy is to determine the density of the stellar and gas disc components. To separate the stellar disc and bulge components, we follow Inoue et al. (2016). We calculate the angular momentum component of each star particle parallel to the angular momentum of the subhalo (J_z) and compare it to the angular momentum of a circular orbit with the same energy ($J_{\rm c}$). Star particles with $J_z/J_{\rm c} < 0.7$ are tagged as bulge stars, and are excluded from our analysis (except for their contribution to the potential and therefore to κ). For gas particles, following Inoue et al. (2016), we include all gas particles within 3 kpc of the disc plane.

Next, we calculate the radial velocity dispersion of the gas and stellar components. For the gas component, we first calculate the local speed of sound ($c_{\rm s}$) and the radial velocity dispersion ($\sigma_{\rm t}$), then calculate the combined $\sigma^2_{\rm gas} = c^2_{\rm s} + \sigma^2_{\rm t}$. As noted by Inoue et al. (2016), $\sigma_{\rm t}$ typically dominates over $c_{\rm s}$. For the stellar component, we simply compute the radial velocity dispersion.

The last component required to calculate $Q_{\rm gas}$ and $Q_{\rm star}$ is the epicyclic frequency (κ) that is defined in terms of the local rotation velocity (v_ϕ) and radius (R).

$$\kappa^2 = 2\frac{v_\phi}{R}\left(\frac{{\rm d}v_\phi}{{\rm d}R} + \frac{v_\phi}{R}\right) \tag{5}$$

Inoue et al. (2016) discuss two possible approaches for measuring κ: separately for gas and stellar components using local rotation velocities or combined for both components using a circular velocity profile ($v_\phi \approx v_{\rm circ} = \sqrt{GM(<r)/r}$). We choose the latter method, as it ensures that κ is never imaginary, therefore allowing us to automate the process of computing Q values for our large ($\sim 10^5$) sample of subhaloes.

To combine $Q_{\rm gas}$ and $Q_{\rm star}$, several methods have been proposed. We follow the method of Romeo & Wiegert (2011). Specifically, for a combined $Q_{\rm 2comp}$:

$$\frac{1}{Q_{\rm 2comp}} = \begin{cases} \frac{W}{Q_{\rm star}} + \frac{1}{Q_{\rm gas}}, & (Q_{\rm star} > Q_{\rm gas}) \\ \frac{1}{Q_{\rm star}} + \frac{W}{Q_{\rm gas}}, & (Q_{\rm star} < Q_{\rm gas}) \end{cases}, \tag{6}$$

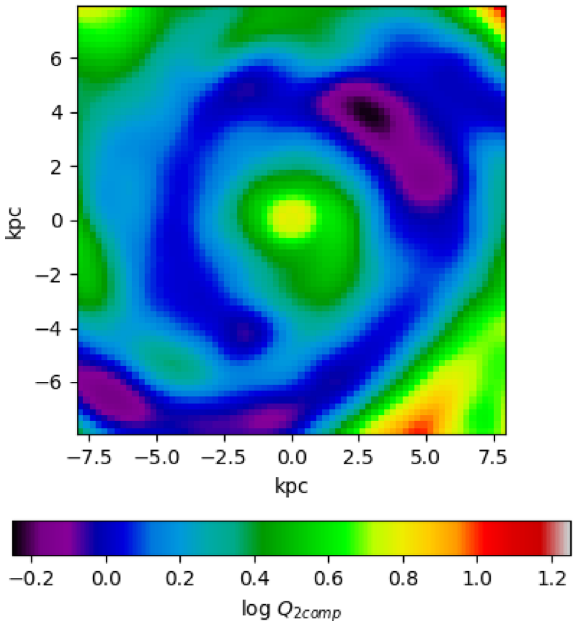

Figure 2. Map of the combined two-component Toomre $Q_{\rm 2comp}$ for an example subhalo (Subfind ID 577184, $z = 0$, $M_* = 10^{10.0}\,{\rm M}_\odot$, sSFR $= 10^{9.6}\,{\rm yr}^{-1}$). Areas of low Q (purple/black) are Toomre unstable.

where

$$W = \frac{2\sigma_{\rm star}\sigma_{\rm gas}}{\sigma^2_{\rm star} + \sigma^2_{\rm gas}}. \tag{7}$$

Fig. 2 shows a map of $Q_{\rm 2comp}$ for an example subhalo. Finally, for quantitative comparison between subhaloes, we reduce each Q map to a single number by computing the baryonic (stellar plus gas) mass fraction within $2R_{\rm e}$ where $Q_{\rm 2comp} < 2$. Using $Q < 1$ instead of $Q < 2$ makes no qualitative differences to our results, however, we chose $Q < 2$ to include all possible regions of instability (Elmegreen 2011).

3 RESULTS

Our goal is to investigate galaxy structural evolution as measured by the relation of stellar mass (M_*) to core stellar density ($\Sigma_{*,2\,\rm kpc}$). We proceed in three steps. First, we check that TNG qualitatively reproduces the observational trends from WE19. Second, we track galaxies back in time and quantify the strength of their core growth by the slope of their evolution in the $\log \Sigma_{*,2\,\rm kpc}$–$\log M_*$ plane. Third, we investigate possible drivers of structural evolution by correlating various galaxy properties with past and future core growth.

3.1 Comparison between TNG and Woo & Ellison (2019)

Our first goal is to check whether TNG reproduces the observed trends under investigation, particularly those presented in WE19. Specifically, we reproduce the $\Sigma_{*,2\,\rm kpc}$–M_* relation and examine how other galaxy properties (AGN fraction, and the gradients of stellar age, sSFR, and gas metallicity) vary as a function of position in the relation. Note that WE19 studied $\Sigma_{*,1\,\rm kpc}$, while we have preferred $\Sigma_{*,2\,\rm kpc}$ for resolution reasons. Therefore, wherever we present a comparison between TNG and the results of WE19, we have replotted their data using $\Sigma_{*,2\,\rm kpc}$, leaving all other aspects of their analysis completely unchanged (qualitatively, the same observational trends are present regardless of whether $\Sigma_{*,1\,\rm kpc}$ or $\Sigma_{*,2\,\rm kpc}$ are used.) Note that although the gradients in the MaNGA sample were not point

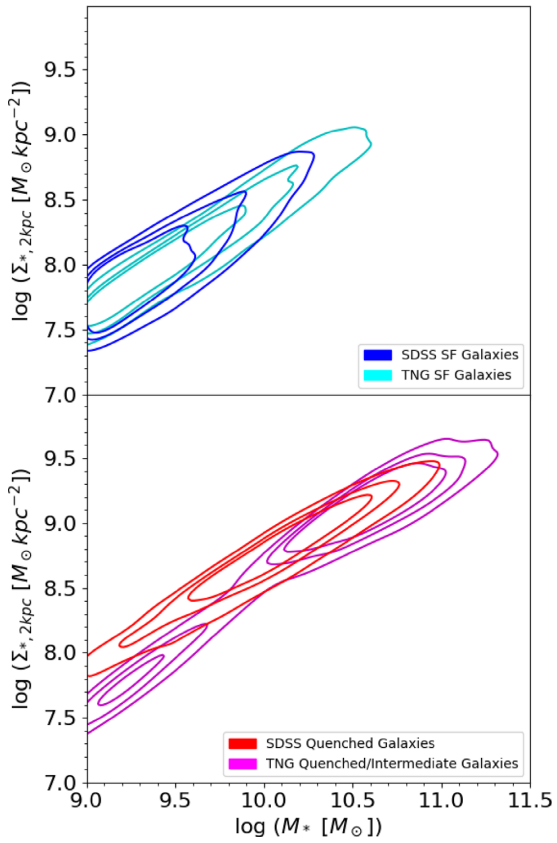

Figure 3. The distribution of isolated galaxies in central stellar mass density ($\Sigma_{*,2\,\mathrm{kpc}}$) versus total stellar mass (M_*) in the SDSS and TNG, split into SF (top) and quenched/intermediate galaxies (bottom). Contour lines represent the same normalized number densities of galaxies for both SDSS and TNG, and are drawn at PDF = 0.1, 0.3, and 0.5. SDSS galaxy densities are corrected for luminosity. SF and Q galaxies in TNG are concentrated at a slightly higher $\Sigma_{*,2\,\mathrm{kpc}}$ and M_*, however, they generally lie on the observed $\Sigma_{*,2\,\mathrm{kpc}}$–$M_*$ relation.

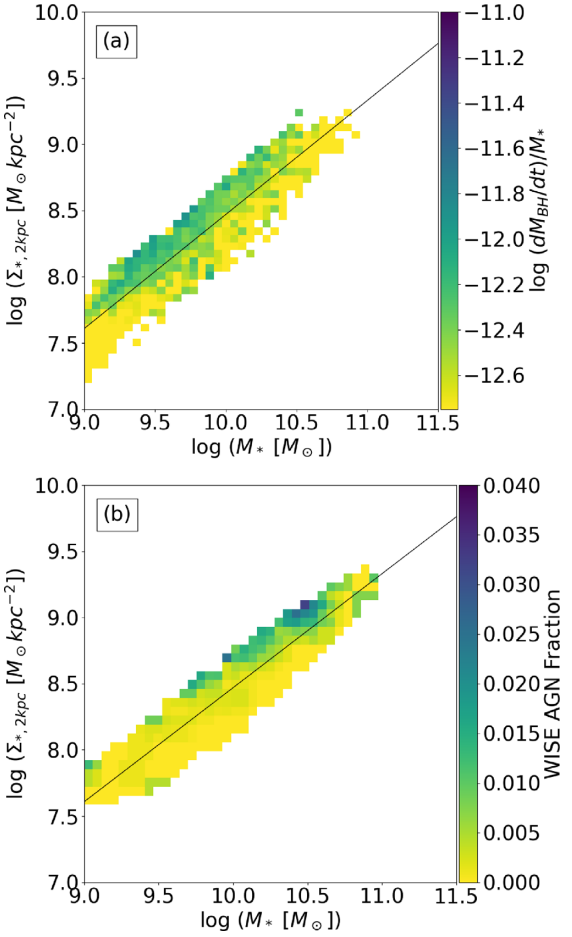

Figure 4. The median BH accretion rate normalized by the stellar mass in TNG (a) and the *WISE*-detected AGN fraction for SDSS SF galaxies (b). Panel (b) is produced following the method of WE19 (their Fig. 10), but using $\Sigma_{*,2\,\mathrm{kpc}}$ instead of $\Sigma_{*,1\,\mathrm{kpc}}$. The line shown, for comparison, is the least-squares fit to the TNG SF subhaloes. TNG shows good agreement, with higher AGN activity at higher $\Sigma_{*,2\,\mathrm{kpc}}$ for a given M_*.

spread function (PSF)-corrected, they were selected to be nearby galaxies for which the PSF full width at half-maximum corresponds to less than 2 kpc in physical size, which is similar to the gravitational softening length in TNG of ∼1 kpc. For more details about the observational analysis, please see WE19.

First, we examine the $\Sigma_{*,2\,\mathrm{kpc}}$–$M_*$ relation for TNG subhaloes, and isolated Sloan Digital Sky Survey (SDSS) galaxies in Fig. 3. The SDSS sample is identical to the sample used in WE19. TNG's distributions of SF and Q galaxies are skewed slightly to higher $\Sigma_{*,2\,\mathrm{kpc}}$ and M_* than SDSS. Otherwise, TNG subhaloes fall on to the observed relations fairly well. We believe the good agreement is the result of at least the following reasons: (1) among several wind models explored for TNG, the fiducial model was chosen to reproduce the observed galaxy stellar size–mass relation at $z = 0$ (Pillepich et al. 2017); (2) galaxy sizes and $\Sigma_{*,2\,\mathrm{kpc}}$ are closely related for SF galaxies (Chen et al. 2020); and (3) the spatial resolution of TNG is roughly the same as that of SDSS, which has a diluting effect on $\Sigma_{*,2\,\mathrm{kpc}}$. We also note that TNG produces a distinct population of low-mass Q subhaloes that appear to have quenched without kinetic mode BH feedback. While interesting, we defer investigation of these low-mass quenched galaxies for future work.

Next, we examine the distribution of AGN activity in the $\Sigma_{*,2\,\mathrm{kpc}}$–$M_*$ plane for SF galaxies only. In WE19, the presence of an AGN was inferred using mid-infrared colours from *WISE*. As a surrogate for AGN strength, we use the total BH accretion rate. When more than one BH particle is present in a subhalo, we sum all the accretion. Although the BH accretion rate does not tell us which mode the AGN is in (kinetic or thermal), the feedback in either case is directly proportional to it. Fig. 4 shows the BH accretion rate (panel a) and the BH mass (panel b), both normalized by M_*, for isolated SF subhaloes, mapped to the $\Sigma_{*,2\,\mathrm{kpc}}$–$M_*$ plane. In all comparisons between observations and TNG (Figs 4–7), we draw a least-squares fit to the TNG SF subhaloes, using randomly projected values for $\Sigma_{*,2\,\mathrm{kpc}}$: $\log(\Sigma_{*,2\,\mathrm{kpc}}) = 0.86(\log M_* - 10.5) + 8.90$. The accretion rate in TNG increases with core density (at fixed M_*), in agreement with the observed AGN fraction from WE19. (Note that Fig. 4 uses the SDSS sample in WE19 rather than the MaNGA sample since spatial information was not needed.)

As a final comparison between simulation and observational trends, we compare radial gradients of stellar age (Fig. 5), sSFR (Fig. 6), and gas metallicity (Fig. 7) in TNG to the results of WE19 using their MaNGA sample. We note that, due to the different methods used to calculate radial gradients, we only compare our results to WE19 qualitatively. The simulated gradients of age and sSFR are in qualitative agreement with the observations. Galaxies with higher core densities (at fixed M_*) have younger stars, and have

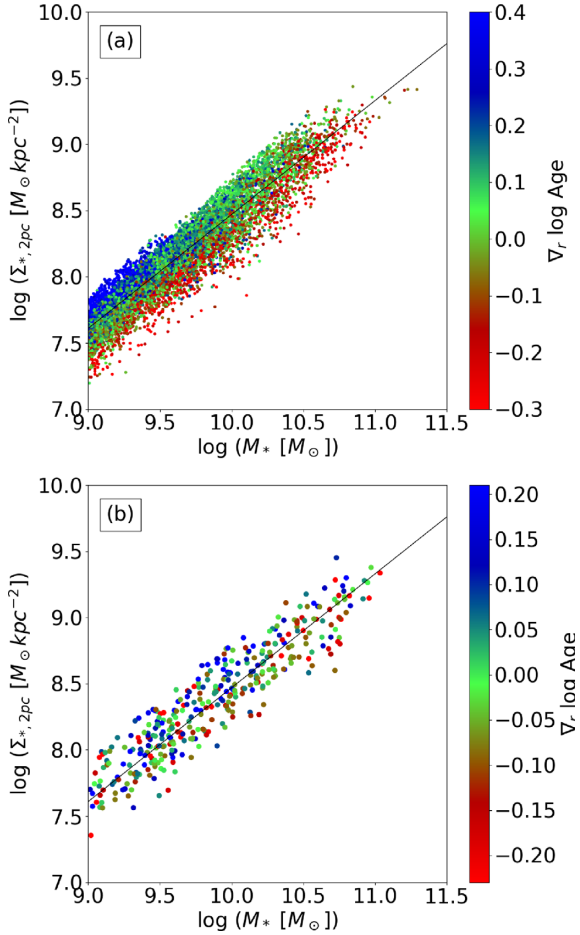

Figure 5. Radial gradients of stellar age in TNG (a) and MaNGA (b) as a function of position in the core density $\Sigma_{*,2\,\mathrm{kpc}}$ versus stellar mass (M_*) plane. Panel (b) is produced following the method of WE19 (fig. 3a), but using $\Sigma_{*,2\,\mathrm{kpc}}$ instead of $\Sigma_{*,1\,\mathrm{kpc}}$. The line shown, for comparison, is the least-squares fit to the TNG SF subhaloes. TNG subhaloes with higher $\Sigma_{*,2\,\mathrm{kpc}}$ at a fixed M_* tend to have younger cores compared to their outskirts, in qualitative agreement with findings from MaNGA.

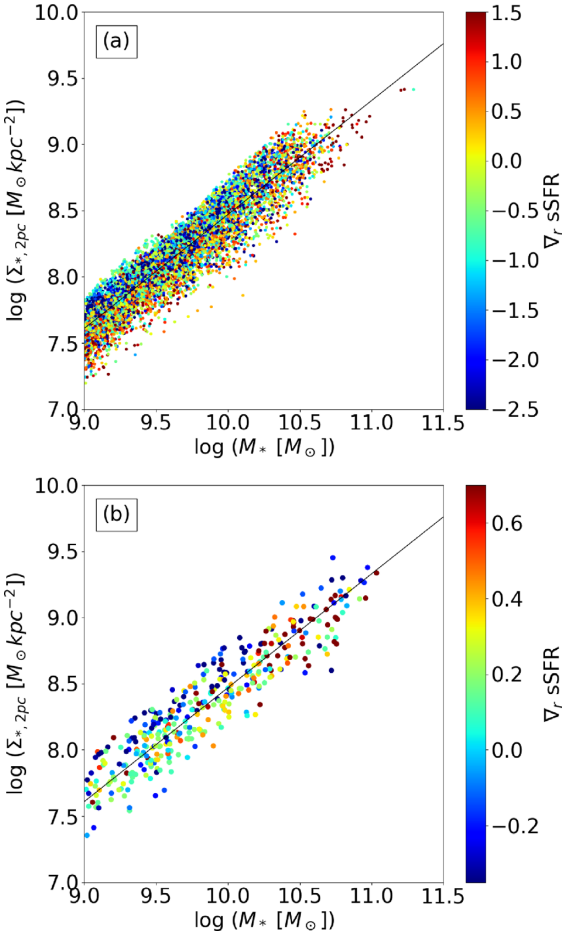

Figure 6. Radial gradients of sSFR in TNG (a) and MaNGA (b) as a function of position in the central stellar density $\Sigma_{*,2\,\mathrm{kpc}}$ versus stellar mass (M_*) plane. Panel (b) is produced following the method of WE19 (fig. 4a), but using $\Sigma_{*,2\,\mathrm{kpc}}$ instead of $\Sigma_{*,1\,\mathrm{kpc}}$. The line shown, for comparison, is the least-squares fit to the TNG SF subhaloes. TNG subhaloes with higher $\Sigma_{*,2\,\mathrm{kpc}}$ at a fixed M_* tend to have centrally concentrated sSFR, in qualitative agreement with findings from MaNGA.

elevated sSFR in their cores. TNG produces a weak radial trend in metallicity gradient, with flatter gradients at higher $\Sigma_{*,2\,\mathrm{kpc}}$ in agreement with WE19.

3.2 Galaxy history in the $\Sigma_{*,2\,\mathrm{kpc}}$–$M_*$ plane

Having demonstrated that TNG generally reproduces the observed patterns in the $\Sigma_{*,2\,\mathrm{kpc}}$–$M_*$ plane, we next examine the evolution of subhaloes over time to determine why the age and sSFR gradients correlate with $\Sigma_{*,2\,\mathrm{kpc}}$. WE19 hypothesized that galaxies with high $\Sigma_{*,1\,\mathrm{kpc}}$ are undergoing a compaction-like process that brings gas towards the centre of the galaxy, increasing the central sSFR, lowering the mean stellar age, and increasing $\Sigma_{*,1\,\mathrm{kpc}}$. In contrast, galaxies with shallow (or positive) sSFR gradients do not build $\Sigma_{*,2\,\mathrm{kpc}}$ as quickly as their total mass. As a result, the evolutionary paths of galaxies in the $\Sigma_{*,2\,\mathrm{kpc}}$–$M_*$ diagram are expected to be shallower for those galaxies with low $\Sigma_{*,2\,\mathrm{kpc}}$, and steeper for those with higher $\Sigma_{*,2\,\mathrm{kpc}}$. These expectations can be tested directly in TNG.

In this work, we study galaxy evolution in the $\Sigma_{*,2\,\mathrm{kpc}}$–$M_*$ diagram in two ways. First, we examine the evolution of subhaloes as a population. Second, we track the evolution of individual subhaloes. Fig. 8 shows the evolution of TNG subhaloes in the $\Sigma_{*,2\,\mathrm{kpc}}$–$M_*$ plane between $z = 2.0$ and $z = 0$. The selection (i.e. isolated SF subhaloes) is repeated at each snapshot. The intercept of the distribution at $M_* = 10^{10.5}$ decreases by ∼0.2 dex between $z = 2.0$ and $z = 0.5$ (10 and 5 Gyr ago), in agreement with results from observations for $\Sigma_{*,1\,\mathrm{kpc}}$ (Barro et al. 2017; Chen et al. 2020). The slope of the relation also decreases with decreasing redshift over this time (by ∼ 0.1, or 10 per cent). Although small, this flattening is statistically significant and disagrees with observations, which show a roughly constant slope (Barro et al. 2017; Chen et al. 2020). In this case, we are comparing $\Sigma_{*,2\,\mathrm{kpc}}$ trends from TNG to $\Sigma_{*,1\,\mathrm{kpc}}$ trends from observations. However, we did check $\Sigma_{*,1\,\mathrm{kpc}}$ in TNG and obtain the same trends as with $\Sigma_{*,2\,\mathrm{kpc}}$. We discuss the implications of TNG's evolving slope of the $\Sigma_{*,2\,\mathrm{kpc}}$–$M_*$ relation in Section 4.

We now shift focus to individual galaxies. As described in Section 2.5, we trace the histories of $z = 0$ galaxies up to $z = 0.5$. Fig. 9 shows the evolutionary histories of 9308 $z = 0$ isolated SF subhaloes in the $\Sigma_{*,2\,\mathrm{kpc}}$–$M_*$ plane. The three panels represent three groups divided by their final ($z = 0$) value of $\Sigma_{*,2\,\mathrm{kpc}}$ relative to the least-squares fit in log $\Sigma_{*,2\mathrm{kpc}}$–log M_* for all SF subhaloes, using face-on

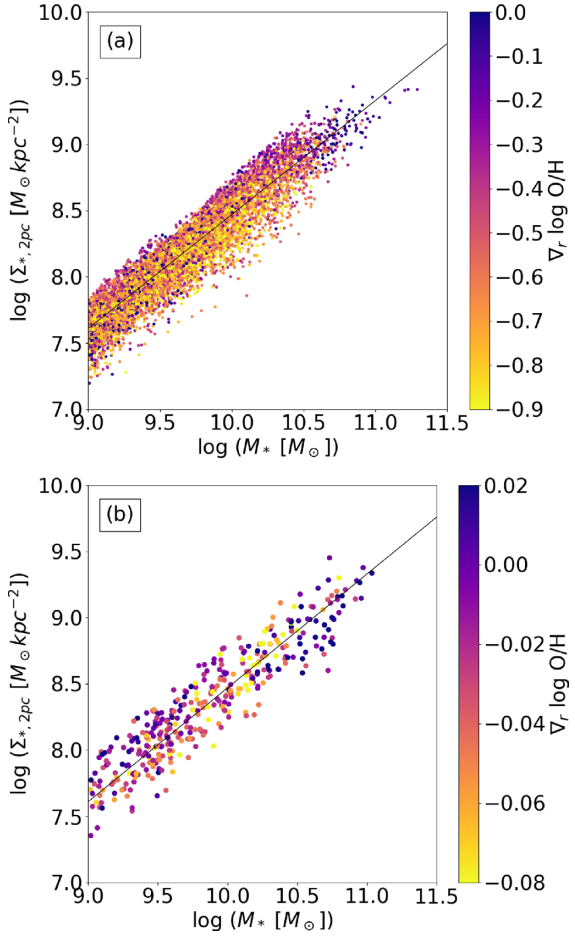

Figure 7. Radial gradients of gas metallicity in TNG (a) and MaNGA (b) as a function of position in the core density $\Sigma_{*,2\,\mathrm{kpc}}$ versus stellar mass (M_*) plane. Panel (b) is produced following the method of WE19 (fig. 5a), but using $\Sigma_{*,2\,\mathrm{kpc}}$ instead of $\Sigma_{*,1\,\mathrm{kpc}}$. The line shown, for comparison, is the least-squares fit to the TNG SF subhaloes. TNG subhaloes with higher $\Sigma_{*,2\,\mathrm{kpc}}$ at a fixed M_* tend to have flatter gradients in gas metallicity, in rough agreement with findings from MaNGA.

values for $\Sigma_{*,2\,\mathrm{kpc}}$. The line used is $\log(\Sigma_{*,2\,\mathrm{kpc}}) = 0.82(\log M_* - 10.5) + 8.80$. Note that this is slightly different than the fit reported in Section 3.1, which used randomly projected values for $\Sigma_{*,2\,\mathrm{kpc}}$ instead of face-on values. We split our sample into subhaloes with dense (high $\Sigma_{*,2\,\mathrm{kpc}}$, Fig. 9a), average (Fig. 9b), and diffuse (low $\Sigma_{*,2\,\mathrm{kpc}}$, Fig. 9c) cores for a given M_*. For visual clarity, each figure only shows a random sample of 100 subhaloes, with each subhalo's history coloured randomly for ease of viewing.

We make two observations from Fig. 9. First, the slopes of the individual tracks are steepest in panel (a) and shallowest in panel (c). *Galaxies with dense cores have steeper evolutionary paths in $\Sigma_{*,2\,\mathrm{kpc}}$–$M_*$ than galaxies with diffuse cores.* This confirms WE19's interpretation of sSFR and stellar age gradients in MaNGA. Second, at low M_* ($\lesssim 10^{9.5}$ $\mathrm{M}_\odot$), some galaxies follow much steeper trajectories indicating strong core growth relative to overall growth.

To quantify these observations, we measure the average slopes of the evolutionary tracks in the $\Sigma_{*,2\,\mathrm{kpc}}$–$M_*$ plane. The slopes are taken linearly between each subhalo's state at $z = 0.5$ and $z = 0$. These slopes correspond to the degree of compaction the subhalo underwent: i.e. subhaloes with steeper slopes grew their cores faster relative to their total stellar mass than those with shallower slopes.

Fig. 10 shows two histograms of the slopes, split by total stellar mass at $M_* = 10^{9.5}$ $\mathrm{M}_\odot$ to highlight the steeper evolutionary slopes possible at low M_* (Figs 9a and b). We further split each histogram based on $\Sigma_{*,2\,\mathrm{kpc}}$ at $z = 0$, using the same three divisions used in Fig. 9: dense cores (blue), average cores (green), and diffuse cores (red). Larger values of slope (x-axis) indicate stronger stellar core growth (compared with overall stellar mass growth).

Fig. 10 demonstrates the mass dependence of the evolutionary slopes, especially for galaxies with denser cores. Galaxies less massive than $10^{9.5}$ $\mathrm{M}_\odot$ evolve more steeply in $\Sigma_{*,2\,\mathrm{kpc}}$–$M_*$ than more massive galaxies. We suspect that the mass dependence of the core growth trajectories may be a resolution effect linked to weaker BH feedback in the less massive galaxies. We confirm that in the lower resolution simulation TNG100-2, the steeper tracks extend to higher masses.

Second, Fig. 10 shows that at all masses, *galaxies with denser cores (blue histogram) at $z = 0$ evolve along steeper trajectories in the $\Sigma_{*,2\,\mathrm{kpc}}$–$M_*$ plane compared to galaxies with diffuse cores (grey histogram).* Third, most (∼65 per cent) subhaloes with $M_* > 10^{9.5}$ $\mathrm{M}_\odot$ evolve along slopes that are shallower than the slope of the single-snapshot distribution fit line of 0.82. In fact, the overall median slope between $z = 0.5$ and $z = 0$ of isolated SF subhaloes with $M_* > 10^{9.5}$ $\mathrm{M}_\odot$ is only 0.63. In other words, the median galaxy does not evolve parallel to the overall distribution at any single snapshot, but rather follows a more shallow trajectory.

We note that a small proportion of galaxies have slightly negative slopes. In these cases, the density of stars in their inner 2 kpc actually decreased as they grew in overall M_*. This could be due to stellar evolution and death, numerical effects (integration errors over time, misplaced subhalo centre points after disruptions, etc.), or also some adiabatic expansion (see e.g. Wellons et al. 2016).

3.3 The drivers of structural evolution

Having shown that galaxies with different evolutionary histories preferentially populate unique regimes in the $\Sigma_{*,2\,\mathrm{kpc}}$–$M_*$ plane, we next investigate the possible drivers of these distinct evolutionary trajectories. Our objective is to test why some subhaloes have an excess of gas that leads to core growth. In particular, we investigate the role of the sSFR gradients, mergers, disc instabilities, BH feedback, and the angular momentum of accretion on galaxy core growth. We quantify the core growth using the average slope of the evolutionary track on the $\Sigma_{*,2\,\mathrm{kpc}}$–$M_*$ diagram over the last 2 Gyr or 4 Gyr and correlate this slope with the desired property at the start and end points of the track. To increase our sample size and achieve more robust statistical results, we consider '$z = 0$' to include subhaloes from snapshots up to $z = 0.05$ (five snapshots total). In other words, we take five different evolutionary segments from each galaxy and treat them as distinct data points. This produces consistent results to analysing only the last snapshot of subhaloes, but with smoother trends.

The effects of galaxy mergers are treated slightly differently as detailed in Section 3.3.2.

3.3.1 The sSFR gradient and core buildup

The observation that galaxies with dense cores have centrally elevated sSFR led WE19 to suggest that central star formation increases the density of the core and leads to steep evolutionary paths in the $\Sigma_{*,2\,\mathrm{kpc}}$–$M_*$ diagram. Indeed, we expect most drivers of core buildup to create a negative sSFR gradient, leading to increased $\Sigma_{*,2\,\mathrm{kpc}}$. The

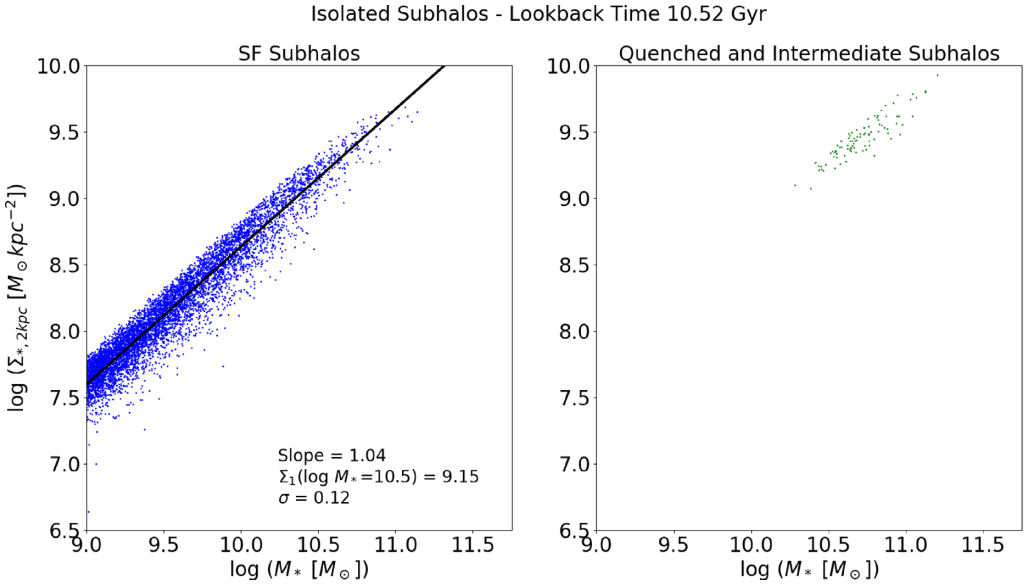

Figure 8. Animation of the distribution of isolated subhaloes in core density $\Sigma_{*,2\,\mathrm{kpc}}$ versus stellar mass (M_*) between $z = 2$ and $z = 0$. The parameters of a least-squares fit to the SF subhaloes, and the residual standard deviation are shown in the bottom right corner of the left-hand panel. As subhaloes transition to quiescence they appear in the right-hand panel. The slope of the fit decreases with decreasing redshift, in contrast to observations, which show a roughly constant slope. Otherwise, TNG qualitatively reproduces the extent and intercept of the SF and Q relations fairly well back to at least $z = 2.0$. The animation embedded in this PDF file can be viewed in Adobe Reader.

only other possibility would be inwards migration of stars, which we expect to be rare. In other words, we expect that the sSFR gradient is the *mechanism* by which other fundamental drivers determine galaxy evolution in $\Sigma_{*,2\,\mathrm{kpc}}$–$M_*$.

We test this explicitly in Fig. 11 (left) where we show the average slope of the evolutionary path in $\Sigma_{*,2\,\mathrm{kpc}}$–$M_*$ as a function of the sSFR gradient at the start (blue) and end (orange) of the 2-Gyr evolutionary track. The right-hand panel shows the same, but over a time interval of 4 Gyr. The blue curves of Fig. 11 show that at the start of the evolutionary tracks, the sSFR gradient correlates weakly with the subsequent growth of the core. Galaxies with positive sSFR gradients ∼2 Gyr ago (SF occurs in the outskirts) were somewhat more likely to grow their total mass more than their cores (shallower evolutionary paths). However, the right-hand panel shows that correlation between core growth and sSFR gradient weakens the farther back we measure the sSFR gradient, virtually disappearing for sSFR gradients measured 4 Gyr ago.

If we look instead at the sSFR gradients at the *end* of the evolutionary tracks (the orange curves), the sSFR gradient correlates more strongly with the past growth of the core. This correlation between the end-point sSFR gradient and core growth also weakens for longer time intervals, but does not disappear after 4 Gyr. In other words, *the current sSFR gradient is an indicator of past core evolution* (over at least 4 Gyr), but past sSFR gradient is not a major predictor of future core growth.

3.3.2 *Galaxy mergers*

Galaxy mergers are a strong candidate for driving core growth. Simulations predict that major mergers can trigger central starbursts (e.g. Cox et al. 2008, Moreno et al. 2015). However, because we select isolated subhaloes at $z = 0$, only a small fraction of our sample (∼10 per cent) have had major mergers since $z = 0.5$. For those subhaloes that did undergo major mergers during this period, we examine the effect the merger had on their evolution in the $\Sigma_{*,2\,\mathrm{kpc}}$–$M_*$ plane. We quantify the core growth (by slope in $\Sigma_{*,2\,\mathrm{kpc}}$–$M_*$) in a time window $\Delta t_{\mathrm{pre/post}}$ before and after the merger. We then compare the two slopes.

Fig. 12 shows three histograms of the difference in trajectory slopes before and after a merger, where we use a $\Delta t_{\mathrm{pre/post}}$ of four snapshots (∼650 Myr) in three mass bins (we vary $\Delta t_{\mathrm{pre/post}}$ between two and six snapshots and find no major variation in our basic results). We divide our sample of mergers in half based on the gas fraction (f_{gas}) within $2R_{\mathrm{e}}$ of the second most massive progenitor immediately prior to the merger (bottom two frames of Fig. 12). The median value of f_{gas} for our sample is 0.40. We also tried dividing based on the total gas fraction of the first two most massive progenitors, as well as using the total bound gas fraction, and found no substantive difference. Mergers are generally wetter at lower M_*. Based on our criteria, 68 per cent of low-mass, 51 per cent of mid-mass, and only 20 per cent of high-mass mergers are 'wet'.

Fig. 12 shows that whether or not mergers are likely to induce rapid core growth is mass and f_{gas} dependent. Wet mergers, on average, lead to increased core growth at all masses. Lower mass galaxies experience a stronger effect. Dry mergers have less effect, with high-mass ($M_* \gtrsim 10^{10}\,\mathrm{M}_\odot$) dry mergers actually resulting in shallower evolutionary trajectories. However, since mergers are rare overall, they are unlikely to be the main driver of rapid core growth in the isolated galaxy population.

3.3.3 *Disc instability and core buildup*

Another candidate for driving the structural evolution of isolated galaxies is the instability of the disc components (both stellar and gas). Disc instabilities lead to fragmentation into clumps of star formation, and the inflow of SF gas towards the galaxy centre, resulting in the build-up of the core (Dekel & Burkert 2014; Zolotov et al. 2015; Inoue et al. 2016).

To investigate disc instability as a driver of core build-up, we construct maps of the Toomre Q parameter (on a resolution scale

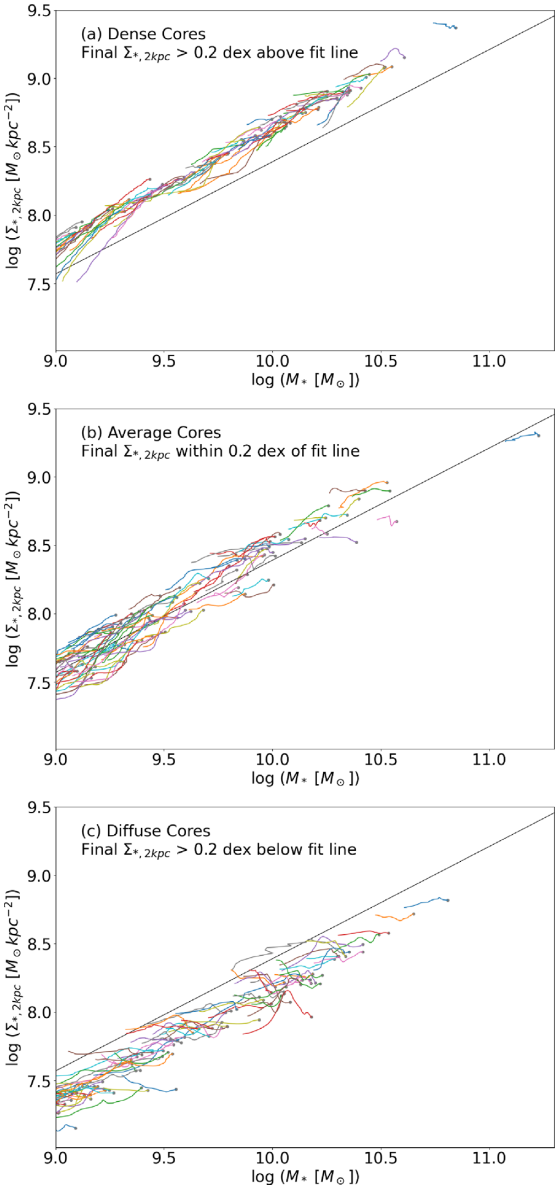

Figure 9. The evolutionary trajectories of example TNG galaxies in the core density $\Sigma_{*,2\,\mathrm{kpc}}$ versus stellar mass (M_*) plane. The trajectories trace the histories of 100 subhaloes that end their evolution with high (panel a), intermediate (panel b), and low (panel c) $\Sigma_{*,2\,\mathrm{kpc}}$ relative to their total M_*. Galaxies are randomly coloured for ease in distinguishing individual trajectories. Galaxies with denser cores (a) generally grow along steeper trajectories than those with diffuse cores (c). At low mass, some galaxies grow very steeply (panel a, $M_* < 10^{9.5}$ $\mathrm{M}_\odot$). The line, for visual reference, is a least-squares fit to all isolated SF subhaloes at $z = 0$ (using face-on values for $\Sigma_{*,2\,\mathrm{kpc}}$) and is identical in all panels. For visual clarity in this figure, we smooth the $\Sigma_{*,2\,\mathrm{kpc}}$ values over time using a Gaussian kernel with a width of two snapshots.

of 0.74 kpc) for each subhalo and its main progenitors. We then compute the fraction of mass within $2R_e$ that is Toomre unstable, i.e. with $Q < 2$ (as discussed in detail in Section 2.6). We also try using R_e instead of $2R_e$ and using a cut-off Q of 1 instead of 2, and in all cases obtain similar results.

Fig. 13 shows the correlation of evolutionary slopes in $\Sigma_{*,2\,\mathrm{kpc}}$–$M_*$ with the unstable mass fraction at the start (blue) and at the end (orange) of evolution segments of 2 Gyr (the results are similar

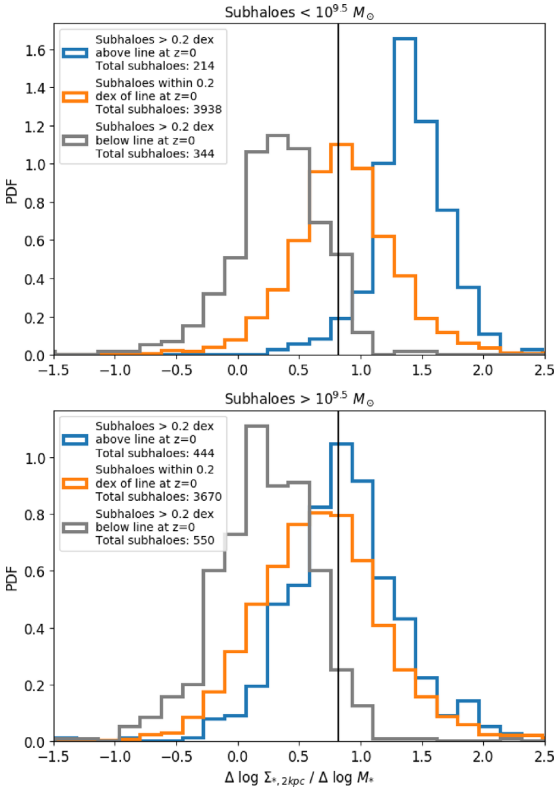

Figure 10. Distributions of the average slope of galaxy trajectories on the core-density $\Sigma_{*,2\,\mathrm{kpc}}$ versus stellar mass (M_*) plane. The panels show isolated SF subhaloes with $M_* < 10^{9.5}$ $\mathrm{M}_\odot$ (top) and $M_* > 10^{9.5}$ $\mathrm{M}_\odot$ (bottom). The trajectories track the MPB from $z = 0.5$ to $z = 0$. The black vertical line at 0.82 marks the slope of the entire $\Sigma_{*,2\,\mathrm{kpc}}$–$M_*$ distribution at $z = 0$. Numbers in the legend indicate the total number of subhaloes in each of the six groups.

for 4 Gyr). The blue curve shows that the unstable mass fraction at the start of the evolution has almost no predictive power on the steepness of the core growth in $\Sigma_{*,2\,\mathrm{kpc}}$–$M_*$. In contrast, the orange curve shows that the unstable mass fraction at the end of the evolution correlates negatively with the steepness of core growth. In other words, galaxies that built their cores rapidly over the last 2 Gyr end up with more stable discs. This can be understood as the stabilizing effect of central spheroids as pointed out by Martig et al. (2009) and Gensior, Kruijssen & Keller (2020). Therefore, *disc instabilities are not a strong driver of structural evolution in TNG*. Instead, it is structural evolution that affects the stability of the disc.

3.3.4 Black hole feedback and core buildup

Supermassive BH feedback is another candidate for influencing the structural evolution of isolated galaxies. We expect the growth of the BH to potentially have two opposing effects on $\Sigma_{*,2\,\mathrm{kpc}}$. On the one hand, the growth of the BH should correlate with the growth of $\Sigma_{*,2\,\mathrm{kpc}}$ since the gas inflows that build the latter also feed the former (Fang et al. 2013; Chen et al. 2020). On the other hand, in TNG, BH feedback returns energy and/or momentum to the galactic gas resulting in a suppression of star formation (Pillepich et al. 2017; Weinberger et al. 2018; Nelson et al. 2019; Terrazas et al. 2020; Zinger et al. 2020). Two modes of feedback are implemented in TNG corresponding to a high-accretion or thermal mode that injects energy into the gas cells in the feedback region, and a low-accretion or kinetic mode that injects a momentum boost to the gas (see Weinberger et al.

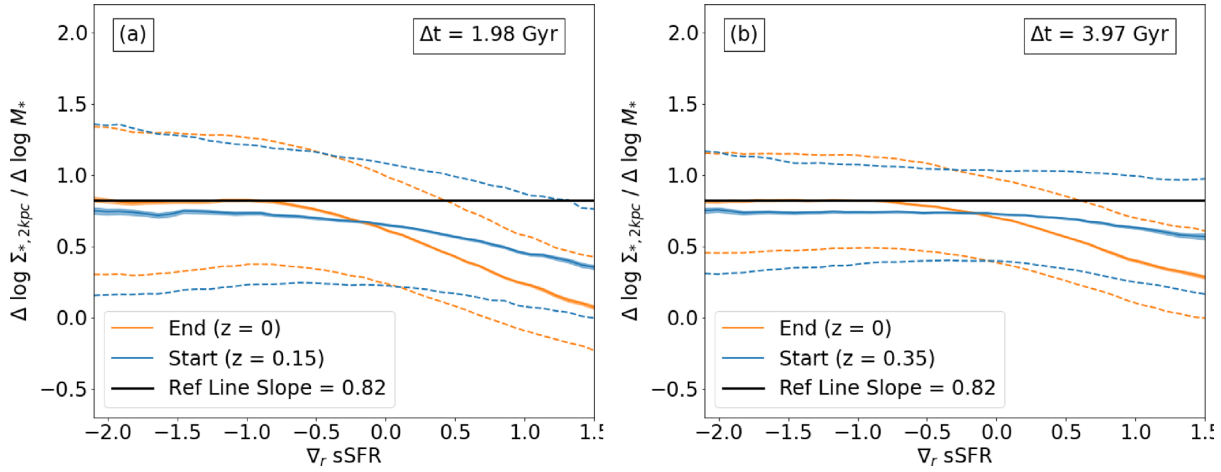

Figure 11. The running median values of the slope of the evolutionary trajectory in the $\Sigma_{*,2\,\mathrm{kpc}}$–$M_*$ plane as a function of galaxy sSFR gradient at the start (blue) and end (orange) of a 1.98 Gyr (left) and 3.97 Gyr (right) trajectory. Quartiles are indicated as dashed lines. The black reference line shows the slope of the least-squares fit to the $\Sigma_{*,2\,\mathrm{kpc}}$–$M_*$ relation at $z = 0$. The sSFR gradient at $z = 0$ is an indicator of *previous* core growth over at least 4 Gyr. However, the sSFR gradient is not a strong predictor of future core growth, with any predictive power disappearing after 4 Gyr.

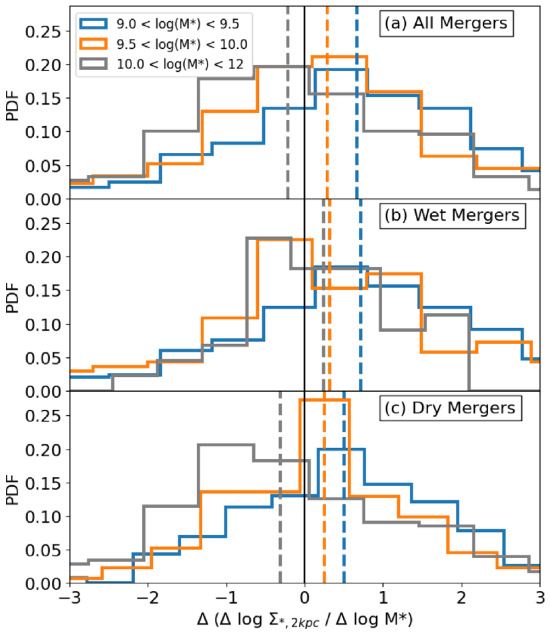

Figure 12. The distribution of trajectory changes after a major merger, where a value of zero (black vertical line) indicates no change. Positive values indicate stronger core growth, whereas negative values indicate weaker core growth, relative to total M_* growth. Vertical dashed lines show median values. Histograms include only isolated SF subhaloes that underwent major mergers since $z = 0.5$. We divide our sample of mergers in half based on the gas fraction (f_{gas}) of the second most massive progenitor: (a) shows all mergers, (b) shows mergers with $f_{\mathrm{gas}} > 0.40$, and (c) shows mergers with $f_{\mathrm{gas}} < 0.40$. Mergers, on average, lead to increased core growth, except for high-mass dry mergers that have slightly the opposite effect. Core growth tends to be slightly stronger at lower mass and higher f_{gas}.

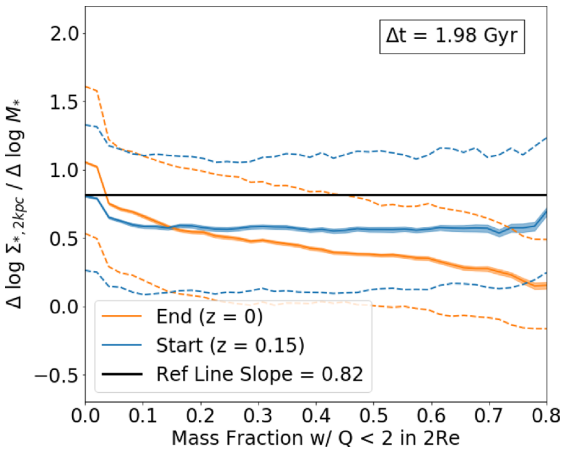

Figure 13. The running median values of the slope of the evolutionary trajectory in the $\Sigma_{*,2\,\mathrm{kpc}}$–$M_*$ plane over the last 1.98 Gyr as a function of the unstable mass fraction at the start (blue) and end (orange) of the trajectory. Quartiles are indicated by the dashed lines. The black reference line shows the slope of the least-squares fit to the $\Sigma_{*,2\,\mathrm{kpc}}$–$M_*$ relation at $z = 0$. Disc instability ∼2 Gyr ago has no significant predictive power for core growth. However, more rapid core growth over the last 2 Gyr predicts more stable discs today.

2018; Zinger et al. 2020 for details). The feedback region is 2–3 kpc in size, so even if the feedback does not succeed in quenching the entire galaxy (quenching seems primarily due to the kinetic mode; Weinberger et al. 2018; Terrazas et al. 2020), BH feedback plausibly suppresses core growth, even if star formation continues outside the feedback region.

We note with caution that in TNG, BH masses for SF galaxies are too massive compared to observed BH masses by almost 2 orders of magnitude (see the top left panel of fig. 7 in Terrazas et al. 2020). For example, TNG predicts that an SF galaxy comparable in mass to the Milky Way should have a supermassive BH of mass $\gtrsim 10^{8.5}\,\mathrm{M}_\odot$ compared to the Milky Way's BH of $\sim 10^{6.6}\,\mathrm{M}_\odot$ (Ghez et al. 2008; Genzel, Eisenhauer & Gillessen 2010). So although the M_{BH}–M_* relation is reproduced for the Q population (Pillepich et al. 2017), BHs seem to grow too quickly in SF galaxies. Nevertheless, we explore the effect of TNG's feedback implementation on the growth of the galaxy core.

We examine the effects of BH feedback in Fig. 14 that shows the steepness of the core growth in $\Sigma_{*,2\,\mathrm{kpc}}$–$M_*$ over 2 Gyr (left) and 4 Gyr (right) as a function of the instantaneous BH mass accretion rate $\dot{M}_{\mathrm{BH}}$, normalized by M_*, at the start (blue) and end (orange) of

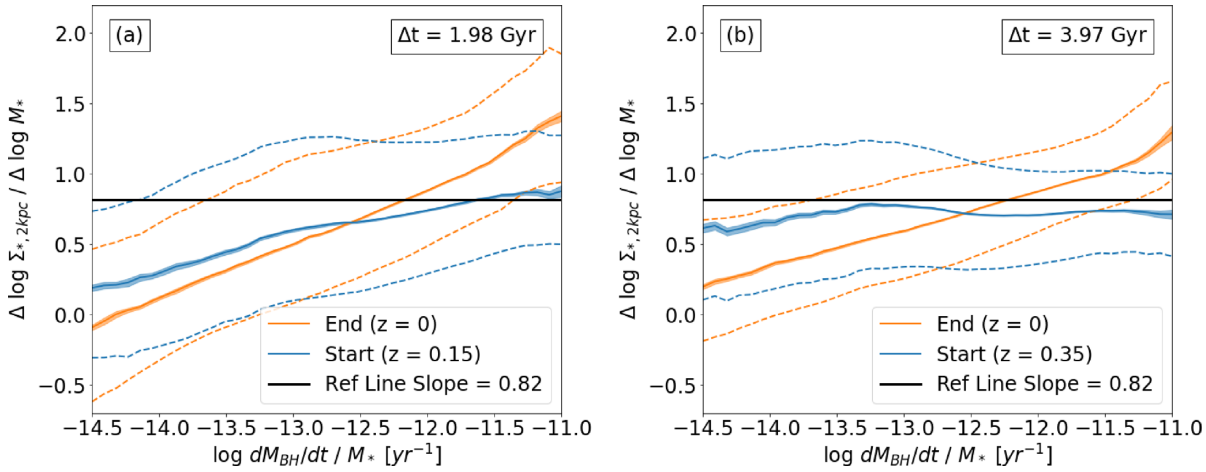

Figure 14. The running median values of the slope of the evolutionary trajectory in the $\Sigma_{*,2\,\mathrm{kpc}}$–$M_*$ plane as a function of the normalized BH accretion rate at the start (blue) and end (orange) of a 1.98 Gyr (left) and 3.97 Gyr (right) trajectory. Quartiles are indicated by the dashed lines. The black reference line shows the slope of the least-squares fit to the $\Sigma_{*,2\,\mathrm{kpc}}$–$M_*$ relation at $z = 0$. The instantaneous BH accretion rates are an indicator of past core growth over at least 4 Gyr. However, the BH accretion rate is not a strong predictor of future core growth, with any predictive power disappearing after 4 Gyr.

the evolution. The BH accretion rate measured at the start of a 2 Gyr evolutionary track predicts the future steepness of the core growth in that track (blue curve of the left-hand panel). However, the correlation weakens for longer time intervals, almost disappearing for 4 Gyr long evolution (blue curve of the right-hand panel). On the other hand, the orange curves show that the BH accretion rate measured at the end of the evolution is a stronger indicator of past core growth: higher accretion rates indicate that the galaxy grew its core density quickly relative to its total mass. This correlation also weakens for longer time intervals, but does not disappear after 4 Gyr. Therefore, we conclude that *the BH accretion rate is an indicator of past core growth* but not a predictor of future core growth. The results shown in Fig. 14 support the scenario in which gas inflows build the core and feed the BH.

Perhaps it is not unexpected that the BH accretion rate does not predict future core growth since it is an instantaneous quantity that varies considerably on rapid time-scales. Terrazas et al. (2020) found that BH feedback is best seen as a cumulative effect, particularly when studying galaxy quenching. Therefore, we also investigated whether the evolution of the core depends on M_{BH}/M_*.[1] In Fig. 15, we show the dependence of the slope of the $\Sigma_{*,2\,\mathrm{kpc}}$–$M_*$ evolution over 2 Gyr on M_{BH}/M_* at the beginning (blue) and at the end (orange) of the evolution (the 4 Gyr interval is similar). The blue curve shows that the normalized BH mass M_{BH}/M_* is somewhat predictive of subsequent core growth. Galaxies with less massive BHs tend to grow their cores rapidly compared to their total mass growth.

The predictive power of M_{BH}/M_* over subsequent core evolution is mass dependent. In Fig. 16, we show the same correlations as Fig. 15, except split by galaxy mass (above and below $10^{10}\,\mathrm{M}_\odot$). Fig. 16 shows that the correlation between M_{BH}/M_* and the steepness of core growth is driven by the low-mass galaxies. For galaxies more

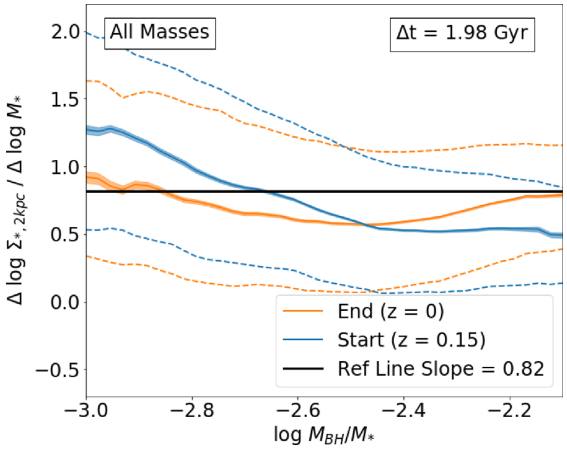

Figure 15. The running median values of the slope of the evolutionary trajectory in the $\Sigma_{*,2\,\mathrm{kpc}}$–$M_*$ plane over the last 1.98 Gyr as a function of the normalized BH mass at the start (blue) and end (orange) of the trajectory. Quartiles are indicated by the dashed lines. The black reference line shows the slope of the least-squares fit to the $\Sigma_{*,2\,\mathrm{kpc}}$–$M_*$ relation at $z = 0$. The BH mass ∼2 Gyr ago predicts subsequent core growth for galaxies.

massive than $10^{10}\,\mathrm{M}_\odot$, BH mass no longer predicts how fast the core grows. This mass dependence roughly corresponds to the mass scale above which the feedback mode switches from thermal to kinetic, the latter being the primary feedback that suppresses star formation. Fig. 17 shows the distribution of BHs and their cumulative kinetic feedback in the $\Sigma_{*,2\,\mathrm{kpc}}$–$M_*$ plane. Kinetic feedback dominates above the same characteristic M_* where steeper core evolutions cease (Figs 9 and 10). At low masses, the thermal mode fails to prevent star formation in the core and $\Sigma_{*,2\,\mathrm{kpc}}$ can grow rapidly compared to M_*.

The results from Figs 14 to 17 together suggest that although instantaneous BH feedback is a poor predictor of core growth, *the cumulative BH feedback history may be suppressing rapid core growth* seen in isolated SF galaxies below $M_* \sim 10^{9.5}\,\mathrm{M}_\odot$. This may also explain the merger stellar mass effect seen above.

[1] M_{BH}/M_* is physically similar to the quantity $\int \dot{E}_{\mathrm{kinetic}}\mathrm{d}t/E_{\mathrm{bind}}$, i.e. the integral of the kinetic energy injected by the BH divided by the binding energy of the gas, which was found by Terrazas et al. (2020) to be the critical quantity for galaxy quenching. We have found as yet unexplained problems with the binding energies for ∼15 per cent of the galaxies (confirmed by B. Terrazas, private communication), and so opted to use the simpler M_{BH}/M_*.

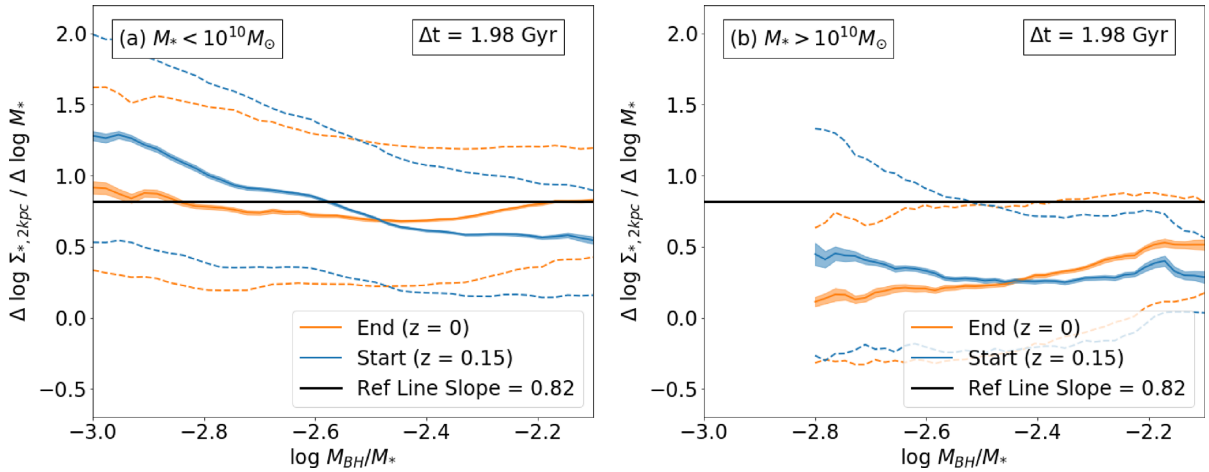

Figure 16. The running median values of the slope of the evolutionary trajectory in the $\Sigma_{*,2\,\mathrm{kpc}}$–$M_*$ plane over the last 1.98 Gyr as a function of the normalized BH mass at the start (blue) and end (orange) of the trajectory. Quartiles are indicated by the dashed lines. The left-hand and right-hand panels show galaxies below and above $M_* = 10^{10}\,\mathrm{M}_\odot$. The black reference line shows the slope of the least-squares fit to the $\Sigma_{*,2\,\mathrm{kpc}}$–$M_*$ relation at $z = 0$. The correlation between BH mass and core growth is driven by the low-mass galaxies. Massive galaxies show very little correlation (where statistics are sufficient).

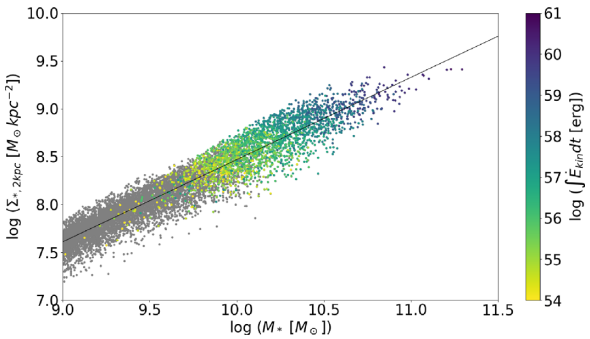

Figure 17. Isolated SF subhaloes in the $\Sigma_{*,2\,\mathrm{kpc}}$–$M_*$ plane, coloured by $\int \dot{E}_{\mathrm{kinetic}} \mathrm{d}t$. Grey dots indicate that the subhaloes' BHs have not produced any feedback in kinetic mode. Note the mass dependence, with kinetic mode BHs becoming prolific above $M_* \sim 10^{9.5}$–$10^{10}\,\mathrm{M}_\odot$.

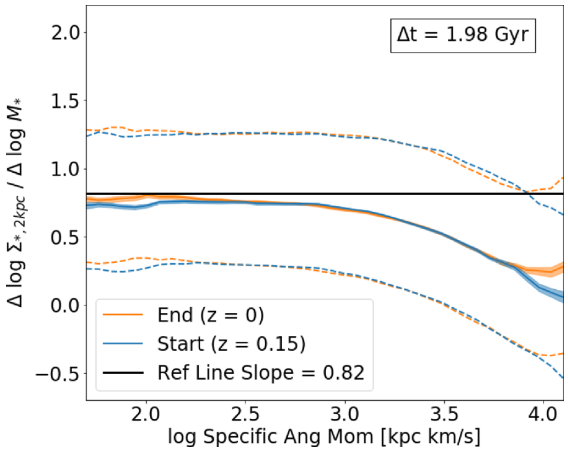

Figure 18. The running median values of the slope of the evolutionary trajectory in the $\Sigma_{*,2\,\mathrm{kpc}}$–$M_*$ plane over the last 1.98 Gyr as a function of the specific angular momentum of accreting gas as measured at half the virial radius at the start (blue) and end (orange) of the trajectory. Quartiles are indicated as dashed lines. The black reference line shows the slope of the least-squares fit to the $\Sigma_{*,2\,\mathrm{kpc}}$–$M_*$ relation at $z = 0$. Higher specific angular momentum of accreting gas ∼2 Gyr ago predicts slower core growth compared to the total mass. This correlation is maintained even when the specific angular momentum is measured at the end of the trajectory indicating that the link between angular momentum and core growth is long lived.

3.3.5 Effects of gas angular momentum

Lastly, we investigate the effect of the angular momentum of the accreting gas on galaxy structural evolution. The angular momentum properties of the gas (which correlate with the angular momentum of the stars and host halo) correlate with galaxy morphology (Fall 1983; Romanowsky & Fall 2012; Zavala et al. 2016; Garrison-Kimmel et al. 2018). Low angular momentum gas can reach the centre of the galaxy and build the core, whereas gas with high angular momentum likely contributes to star formation in the disc.

In order to study the effect of angular momentum on core growth, we calculate the specific angular momentum of gas crossing a shell of $R_{\mathrm{vir}}/2$. The infall time from this point is $\lesssim$1 Gyr. We select gas particles outside this shell with inwards radial velocity such that they would cross the shell within 100 Myr. We check that varying this period from 10 Myr to 1 Gyr has no significant impact on our results.

Fig. 18 shows the correlation between the evolutionary slope in the $\Sigma_{*,2\,\mathrm{kpc}}$–$M_*$ plane and the total specific angular momentum of gas particles at the start (blue) and end (orange) of 2 Gyr of evolution (4 Gyr is similar). As expected, the blue curve shows that subhaloes whose infalling gas had low angular momentum at the start of the evolution will experience steeper evolutionary slopes in the $\Sigma_{*,2\,\mathrm{kpc}}$–$M_*$ plane, and vice versa.

The orange curve of Fig. 18 shows that the gas angular momentum at the end of the evolution also correlates with the steepness of core growth with similar correlation strength as the blue curve. Given that the infalling gas has not yet reached the galaxy, there is no reason to expect a correlation between the end-point angular momentum and the galaxy's core growth, unless the accretion and its angular momentum are sustained over long periods (>2 Gyr) with lasting effect on core growth. Indeed, we confirm that the same correlation between core growth and the total specific angular momentum of the accreting gas (both before and after the evolution) is sustained for at least the last 5 Gyr. Therefore, *structural evolution, namely rapid core growth, is driven by the angular momentum of the accreting gas*.

4 DISCUSSION

4.1 Drivers of galaxy evolution on the $\Sigma_{*,2\,\mathrm{kpc}}$–$M_*$ plane

We have demonstrated that TNG100-1 qualitatively reproduces many observed structural properties, making it a useful tool to investigate the origin of the observed galaxy structure. Using TNG100-1, we are able to answer key questions pertaining to galaxy evolution, for example: why do galaxies with dense cores also have centrally concentrated star formation? What is the history of structural evolution for isolated SF galaxies, and what drives the evolution of the core? These questions were ultimately motivated by the existence of the morphology–quiescence relation, where the density of the core is strongly correlated with quiescence. We defer a treatment of Q galaxies to a later study, while we first attempt to understand the growth of the core in SF galaxies.

In Section 3.3.3, we demonstrated that disc instabilities are not a major driver of structural evolution in isolated galaxies at low-z. There is little correlation between Toomre Q and core growth over the 5 Gyr prior to $z = 0$. In fact, we have found that Toomre Q *responds* to the structural evolution, such that rapid core growth results in more stable discs. Our findings are consistent with the scenario where dispersion-supported central spheroids stabilize galactic discs (Martig et al. 2009; Gensior et al. 2020).

Our findings that disc instabilities are unimportant for low-z core building is in contrast to what is seen in hydrodynamical simulations at high-z ($z \sim 2$; Zolotov et al. 2015). At cosmic 'high-noon', discs are violently perturbed by intense instreaming, which include minor mergers. Minor mergers are not very different from violent disc instabilities since minor mergers occur frequently relative to the disc orbital time. At low-z, mergers are less frequent, especially for isolated galaxies; we have shown here that although mergers tend to lead to core build-up, the effect decreases as galaxy mass increases and gas fraction decreases. At the highest masses, dry mergers actually have the effect of diffusing the core stellar density. This could be due to resolution effects, but could also be due to the fact that in TNG, BH feedback in low-mass galaxies is in the thermal mode that may be ineffective at removing SF gas from the core. However, in galaxies more massive $M_* \sim 10^{10}\,\mathrm{M}_\odot$, the low-accretion kinetic mode is more effective at preventing mergers from funnelling gas to the core.

We find that kinetic BH feedback, particularly at $M_* \gtrsim 10^{9.5}\,\mathrm{M}_\odot$, prevents steep core growth. Choi et al. (2018) recently found similar results in a set of zoom-in simulations using mixed kinetic and thermal AGN feedback, in particular for quenched galaxies. They found that the presence of the AGN halts $\Sigma_{*,1\,\mathrm{kpc}}$ growth as galaxies quench. Further, a combination of stellar death, adiabatic expansion following gas expulsion, and binary BH scouring results in $\Sigma_{*,1\,\mathrm{kpc}}$ decreasing over long times (as they call 'puffing-up' the core).

While BH feedback appears to prevent the most rapid core growth above $M_* \sim 10^{9.5}\,\mathrm{M}_\odot$, the variation in steepness of core growth between subhaloes is governed by the angular momentum of the accreting gas. In the classical picture of galaxy formation, gas is accreted on to the galaxy in a 'hot' mode (cooling from the shock-heated halo), and in a 'cold' mode (dense and filamemtary that does not shock heat), but the angular momentum of both modes should be the same as the halo (e.g. Fall & Efstathiou 1980). The angular momentum of the accretion (and thus also of the halo) correlates with galaxy morphology (Romanowsky & Fall 2012; Teklu et al. 2015; Zavala et al. 2016; Garrison-Kimmel et al. 2018), and by extension with $\Sigma_{*,2\,\mathrm{kpc}}$. However, a more complex and nuanced picture of the relation between angular momentum and the galaxy has also emerged from recent work. For example, cold filaments carrying high angular momentum are able to penetrate the hot halo without mixing with the low angular momentum halo gas, so the accreting gas can have very different angular momentum from the halo (Stewart et al. 2017). The angular momentum of the halo is the cumulative result of past accretion, whereas the cold gas in a halo is recent, entering the halo with higher specific angular momentum (Danovich et al. 2015; Stewart et al. 2017). Thus, it has been recognized that the angular momentum of accreting gas does not neccessarily determine galaxy morphology and core density (Teklu et al. 2015).

Instead, it is the alignment of the angular momentum of the gas with that of the galaxy that correlates most strongly with galaxy morphology (Sales et al. 2012; Duckworth, Tojeiro & Kraljic 2020). The hot low angular momentum gas cooling from halo often contributes significantly to the disc at later times, whereas the high angular momentum cold accretion, which is not generally well aligned with the halo or galaxy at late times, contributes to the spheroids.

In this study, we have used $\Sigma_{*,2\,\mathrm{kpc}}$ as a measure of 'morphology'. $\Sigma_{*,2\,\mathrm{kpc}}$ is tightly correlated with M_*, but galaxies vary considerably in their evolutionary paths along the $\Sigma_{*,2\,\mathrm{kpc}}$–$M_*$ relation. We have shown that the steepness of the evolutionary path in $\Sigma_{*,2\,\mathrm{kpc}}$–$M_*$, i.e. the rate of the growth of the core relative to the growth of the whole galaxy, correlates with the specific angular momentum of the accreting gas. In our analysis, we have included all infalling gas, whether in the cold or hot mode. We have also taken the vector sum of the angular momentum of all infalling gas particles, so that the alignment between cold and hot modes is taken into account. Non-aligned cold gas, even with high angular momentum, will lower the total specific angular momentum, resulting in steeper evolutionary tracks in $\Sigma_{*,2\,\mathrm{kpc}}$–$M_*$. We note that we see the same trends even when using the scalar sum of the angular momentum vectors that may suggest that non-aligned gas may not play an important role in core evolution. Lastly, we note that the correlation between core growth and the total specific angular momentum of the accreting gas is long lived ($\gtrsim$5 Gyr).

Therefore, we have found that in the TNG simulations, the growth of the galaxy core is related to both the mode of BH feedback (thermal versus kinetic), and to the angular momentum of accreting gas. Above $\sim 10^{9.5}\,\mathrm{M}_\odot$, BH feedback slows core growth, but low angular momentum gas successfully overcomes the effects of BH feedback at all masses. In fact, the shallower trajectories of core growth occur at lower $\Sigma_{*,2\,\mathrm{kpc}}$ (relative to M_*; see Figs 9 and 10), where the M_{BH} is lower.

Woo & Ellison (2019) treated the shallower trajectory as the 'default' growing mode (see also Chen et al. 2020). We have seen that these shallow trajectories are due to a combination of high angular momentum accretion and BH feedback. Woo & Ellison (2019) also interpreted the steeper trajectories as a 'compaction-like' event that deviates from the default growing behaviour. We have seen here that steeper tracks (above $\sim 10^{9.5}\,\mathrm{M}_\odot$) are caused by accretion of gas with lower total specific angular momentum, including non-aligned accretion with higher specific angular momentum. Our result that the correlation between low gas angular momentum and steep core build-up is long lived perhaps implies that the steeper trajectories are not necessarily a special event, but rather a result of continuous accretion of low angular momentum or non-aligned material.

Based on these findings, we propose a new cartoon for galaxy evolution in the $\Sigma_{*,N\,\mathrm{kpc}}$–$M_*$ plane (Fig. 19). The slopes are shallower than proposed in the cartoon by Woo & Ellison (2019, see their fig. 2), and include a range of slopes that depend on position in the diagram rather than the two-track evolution they proposed. Nevertheless, the salient point of their proposal is confirmed in TNG: galaxies with

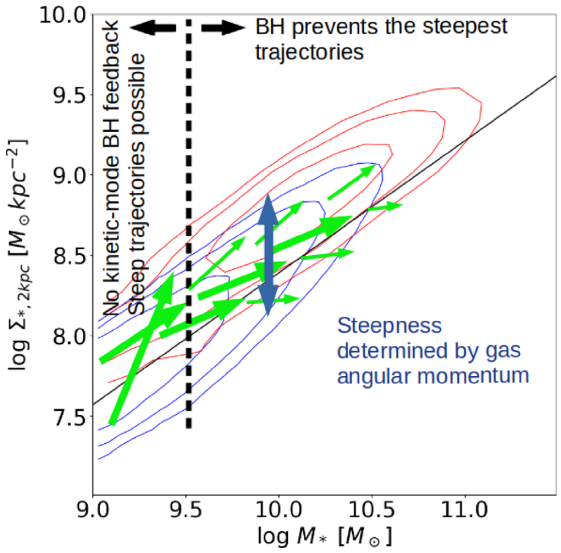

Figure 19. A summary of the evolution of isolated galaxies in the core density $\Sigma_{*,2\,\mathrm{kpc}}$ versus stellar mass (M_*) plane and the drivers of core growth in the TNG simulation, at $z \sim 0$. Green arrows indicate schematic trajectories for individual galaxies. Contours represent number density of SF (blue) and Q (red) galaxies in SDSS (reproducing fig. 2 of WE19, except with $\Sigma_{*,2\,\mathrm{kpc}}$ instead of $\Sigma_{*,1\,\mathrm{kpc}}$). In TNG, galaxies at low mass (left of the dashed black line) have low-mass BHs that do not produce kinetic feedback, allowing steep core growth relative to total M_*. At all masses, galaxies with higher $\Sigma_{*,2\,\mathrm{kpc}}$ by $z = 0$ experienced steeper core growth in the past. Furthermore, the steepness of a galaxy's trajectory in $\Sigma_{*,2\,\mathrm{kpc}}$–$M_*$ is determined primarily by the angular momentum of the infalling gas from the halo. The evolutionary pathways diverge slightly, resulting in a marginally wider distribution over time (Fig. 8). Quenching removes galaxies from the upper envelope of the SF relation, potentially keeping the relation relatively tight. We stress that this cartoon represents TNG behaviour at low redshift, as we have not investigated trajectories or drivers earlier than $z = 0.5$.

diffuse cores at $z = 0$ grew their total mass faster than their cores in the past, while those with dense cores by $z = 0$ grew their cores quickly relative to their total mass. Subhaloes with dense cores mostly grew parallel to the fit line (which is steep relative to the median evolutionary slope), and subhaloes with more diffuse cores relative to their mass mostly grew along shallower evolutionary tracks.

4.2 Implications for the evolution of the $\Sigma_{*,2\,\mathrm{kpc}}$–$M_*$ relation

The zero-point of the $\Sigma_{*,1\,\mathrm{kpc}}$–$M_*$ relation at $M_* = 10^{10.5}\,\mathrm{M}_\odot$ has been observed to increase with z until $z \sim 2$ (Barro et al. 2017; Mosleh et al. 2017). We confirm a similar evolution of the relation in TNG (Fig. 8). However, the individual galaxies evolve upwards and to the right in this diagram (they are always growing both their total masses and their cores). If the evolutionary tracks are shallower than the main relation, the zero-point decreases: perhaps more accurately, the main relation evolves to the right (see Chen et al. 2020). What is driving the shallower trajectories, and thus the observed zero-point evolution? We have found that they are the result of both BH feedback and accreting gas with high angular momentum. Without the accumulated feedback of the massive BHs, even high angular momentum accretion will eventually feed core growth. However, even with massive BHs, high angular momentum accretion is required to produce shallower trajectories of core growth.

Although the observed zero-point evolution of the $\Sigma_{*,2\,\mathrm{kpc}}$–$M_*$ relation is qualitatively reproduced in TNG, the slope of the relation evolves significantly in TNG (i.e. the relation is steeper with z), contrary to the remarkably constant slope in the observed Universe (Saracco, Gargiulo & Longhetti 2012; Tacchella et al. 2015; Barro et al. 2017; Mosleh et al. 2017; Tacchella et al. 2017). Since galaxies growing in the steeper mode of core evolution have average slopes that are comparable to the slope of the relation, this may imply that too many galaxies at high-z in TNG are in the steeper mode of core growth. In other words, either BH feedback is not effective enough in tempering core growth at high-z, or the accreting gas falls in with angular momentum that is too low at high-z. Given the long-lived and slowly evolving nature of cosmic inflows (Stewart et al. 2017), and given the neccessarily simplistic nature of the subgrid implementation of BH feedback in large simulations, we suspect that it is the BH feedback that is to be blame, i.e. the feedback is not effective enough at high-z.

Alternatively, or perhaps in addition to having too many rapidly growing cores at high-z, the evolving slope of the $\Sigma_{*,2\,\mathrm{kpc}}$–$M_*$ relation may be due to TNG having too many galaxies at low-z on the shallow mode of core growth. In other words, either BH feedback is overly effective at stunting core growth at low-z, or the accreting gas falls in with angular momentum that is too high. Similarly, if BHs are too effective at low-z, they may be driving many of the steeply evolving galaxies into quiescence, removing too many with high $\Sigma_{*,2\,\mathrm{kpc}}$ from the $\Sigma_{*,2\,\mathrm{kpc}}$–$M_*$ relation for SF galaxies. Again, we suspect that the BH feedback implementation is the culprit, rather than the gas accretion.

The overall implications of our findings, as well as the relatively tight scatter in the observed $\Sigma_{*,2\,\mathrm{kpc}}$–$M_*$ relation, imply that the BH feedback and the angular momentum of the accreting gas conspire to regulate the growth of galaxy cores in relation to the growth of their total stellar mass. BH feedback and gas accretion seem to act in concert such that the slope of the $\Sigma_{*,2\,\mathrm{kpc}}$–$M_*$ remains constant while the zero-point decreases over time.

4.3 Caveats

We note that all of our findings regarding BH feedback come with the caveat that in TNG, BHs in SF galaxies are too massive by almost 2 orders of magnitude compared with observations. Although the feedback implementation in TNG successfully reproduces the observed BH masses in the Q population, BHs grow too quickly in SF galaxies (see e.g. fig. 7 in Terrazas et al. 2020). It remains to be seen whether the feedback physics in TNG could be scaled to produce lower BH masses in SF galaxies while still successfully quenching galaxies.

We note that our interpretations are based on the assumption that the formation of a dense core must be caused by an inflow of gas, fuelling star formation in the galactic core. The other possibility is that stars migrate inwards. However, apart from mergers or other galaxy interactions, we see no mechanism that could cause this on a significant scale (although slow outward migration of stars can occur as shown by Choi et al. 2018). We have shown that mergers are rare in our sample, and since we have selected only isolated galaxies, we expect other interactions are also rare.

We also note that studying the inner 1–2 kpc of subhaloes is pushing the resolution limit of TNG100-1. In particular, our examination of disc instabilities was limited to a scale of 0.74 kpc. Most SF regions are much smaller (~10–100pc). We acknowledge that the resolution of TNG100-1 does not allow us to probe disc instabilities down to these scales. In this work, we present $\Sigma_{*,2\,\mathrm{kpc}}$ instead of $\Sigma_{*,1\,\mathrm{kpc}}$ due to resolution concerns. We did run all analyses for $\Sigma_{*,1\,\mathrm{kpc}}$ in addition to $\Sigma_{*,2\,\mathrm{kpc}}$ and found all trends were the same.

In TNG, subhaloes exhibit more spread in $\Sigma_{*,1\,\mathrm{kpc}}$ than $\Sigma_{*,2\,\mathrm{kpc}}$, as do galaxies in SDSS and MaNGA. Low-mass subhaloes $< 10^{9.5}\,\mathrm{M}_\odot$ exhibit even steeper growth in $\Sigma_{*,1\,\mathrm{kpc}}$–$M_*$ than in $\Sigma_{*,2\,\mathrm{kpc}}$–$M_*$.

To check for convergence and any effects of resolution, we also ran our analyses on TNG100-2. TNG100-2 has roughly half the spatial resolution of TNG100-1. For example, the gravitational softening length for collisionless particles in TNG100-1 is 0.74 kpc while in TNG100-2 it is 1.48 kpc (Nelson et al. 2019). In general, TNG100-2 produces a similar distribution of SF, intermediate, and Q subhaloes as Fig. 3, with better agreement at $M_* > 10^{10}\,\mathrm{M}_\odot$. The three sequences occupy about the same ranges of M_* as TNG100-1. However, the sequences in TNG100-2 all sit about 0.1–0.2 dex lower in $\Sigma_{*,2\,\mathrm{kpc}}$ and about 0.3–0.4 dex lower in $\Sigma_{*,1\,\mathrm{kpc}}$.

Although we must conclude that TNG100-1 may not be fully converged in $\Sigma_{*,2\,\mathrm{kpc}}$ or $\Sigma_{*,1\,\mathrm{kpc}}$, the trends seen in Figs 4, 5, and 6 are all present in both TNG100-2 and TNG100-1. We also found that subhalo histories were steeper for galaxies that end up with higher $\Sigma_{*,2\,\mathrm{kpc}}$ by $z = 0$, and vice versa (as seen in Fig. 9), in both simulation runs. TNG100-2, however, does not produce the clear limit at $\sim 10^{9.5}$ $\mathrm{M}_\odot$ for steep evolutionary tracks. In terms of correlating slopes of the evolutionary trajectories, TNG100-2 does produce roughly the same trends seen in Fig. 11 (sSFR gradient), Fig. 13 (Toomre Q), and Fig. 14 (BH accretion rate). However, the trends seen in Fig. 15 (BH mass) only agree above $M_* > 10^{10}\,\mathrm{M}_\odot$. The correlation seen in Fig. 18 (angular momentum) is not present in TNG100-2, although we note that the mass resolution of gas particles is an order of magnitude worse than TNG100-1.

We acknowledge that the results presented may therefore not be fully converged. We look forward to the public release of TNG50 to check our results at higher resolution. We present details of our convergence tests in Appendix A.

5 SUMMARY

We use the public data release of IllustrisTNG to investigate the recent morphological evolution of isolated galaxies. Specifically we consider the evolution in core stellar density ($\Sigma_{*,2\,\mathrm{kpc}}$) relative to the evolution in total stellar mass (M_*). Our findings regarding the $\Sigma_{*,2\,\mathrm{kpc}}$–$M_*$ can be summarized as follows:

(i) Qualitatively, TNG produces the observed $\Sigma_{*,2\,\mathrm{kpc}}$–$M_*$ relations for isolated galaxies including the SF and Q sequences (Figs 3 and 8), AGN distribution (Fig. 4), and gradients of SFR (Fig. 5), stellar age (Fig. 6), and gas phase metallicity (Fig. 7).

(ii) The progenitors of galaxies with diffuse cores at $z = 0$ (at fixed M_*) evolve along shallow trajectories in the $\Sigma_{*,2\,\mathrm{kpc}}$–$M_*$ plane. Conversely, the progenitors of galaxies with dense cores at $z = 0$ evolve along steeper evolutionary tracks (Figs 9 and 10). 65 per cent of galaxies with $M_* > 10^{9.5}$ $\mathrm{M}_\odot$ have shallower trajectories than the main distribution in $\Sigma_{*,2\,\mathrm{kpc}}$–$M_*$. Those with dense cores evolve roughly parallel to the main distribution of galaxies. However, low-mass galaxies ($<10^{9.5}$ $\mathrm{M}_\odot$) mostly evolve steeply in the $\Sigma_{*,2\,\mathrm{kpc}}$–$M_*$ plane, likely due to the inability of BH feedback to prevent star formation in the core.

We investigate possible drivers of steep core growth, namely high central sSFR, merging, disc instabilities, weak BH feedback and low angular momentum of accretion. We find that:

i) A galaxy's instantaneous sSFR gradient is an indication of its past core evolution (over the last ∼4 Gyr), such that galaxies with more centrally concentrated sSFR tended to have more rapid core growth relative to the growth of their overall mass. The sSFR gradient in the past is not a major predictor of future core growth (Fig. 11).

ii) Major mergers are rare in isolated galaxies since $z = 0.5$ (10 per cent of our sample). Mergers cause steeper core growth, but the effect decreases with increasing mass and decreasing gas fraction (Fig. 12). Additionally, most mergers at $M_* > 10^{10}\,\mathrm{M}_\odot$ are dry.

iii) Disc instability at a resolution scale of 0.74 kpc (as measured by the fraction of mass with Toomre $Q < 2$) does not predict the evolution of the core (Fig. 13). Rather, steeper core growth in the past predicts more stable discs today, indicating that dense cores have a stabilizing effect on the disc.

iv) High instantaneous BH accretion rate is an indicator of rapid core growth over the past 4 Gyr (relative to the growth of M_*), but the BH accretion rate in the past is not a major predictor of future core growth (Fig. 14). However, the cumulative BH feedback history as measured by M_{BH}/M_* does predict future core growth for low-mass ($M_* \lesssim 10^{9.5}\,\mathrm{M}_\odot$) galaxies (Figs 15 and 16) in the sense that lower M_{BH}/M_* predicts rapid core growth. Low-mass galaxies have low M_{BH}, therefore they tend to feedback in the thermal AGN mode, which couples less effectively with the surrounding gas than kinetic mode. We interpret this as the cause of steeper core growth (Fig. 17). For more massive galaxies ($M_* \gtrsim 10^{9.5}\,\mathrm{M}_\odot$), trajectories in $\Sigma_{*,2\,\mathrm{kpc}}$–$M_*$ are on average shallower than for the less massive galaxies, suggesting that kinetic feedback was suppressing star formation within the feedback region of 2–3 kpc. However, we found no correlation between M_{BH} and core growth for these massive galaxies.

v) The total specific angular momentum of the accreting gas in the halo predicts the steepness of core growth (Fig. 18). Galaxies accreting high angular momentum gas tend to evolve along shallower slopes in the $\Sigma_{*,2\,\mathrm{kpc}}$–$M_*$ plane. Furthermore, this correlation persists whether measuring the angular momentum at the beginning of the evolutionary track or at the end of the track, even after 5 Gyr of evolution. This indicates that the connection between the angular momentum of the accreting gas and the steepness of core growth is long-lived.

The growth of galaxy cores in the TNG model is complex and is related to at least two physical drivers (the angular momentum of gas accretion and the BH feedback). It is entirely plausible that other causal factors that we have not considered are also at play, especially given the large scatter in the correlations presented here.

ACKNOWLEDGEMENTS

We thank the anonymous referee for the insightful comments. We acknowledge the helpful and stimulating discussions with Andi Burkert, Sandy Faber, Nir Mandelker, Dave Patton, Salvatore Quai, Sandro Tacchella, Bryan Terrazas, and Elad Zinger. SLE gratefully acknowledges the receipt of an National Sciences and Engineering Research Council (NSERC) Discovery Grant. MHH acknowledges support from the William and Caroline Herschel Post-doctoral Fellowship fund, and the Vanier Canada Graduate Scholarship.

The simulations of the IllustrisTNG project used in this work were undertaken with compute time awarded by the Gauss Centre for Supercomputing (GCS) under GCS Large-Scale Projects GCS-ILLU and GCS-DWAR on the GCS share of the supercomputer Hazel Hen at the High Performance Computing Center Stuttgart (HLRS), as well as on the machines of the Max Planck Computing and Data Facility (MPCDF) in Garching, Germany.

This research made use of ASTROPY,[2] a community-developed core PYTHON package for Astronomy (Robitaille et al. 2013; Price-Whelan et al. 2018). This research also made use of the computation resources provided by Westgrid (www.westgrid.ca) and Compute Canada (www.computecanada.ca).

Funding for the Sloan Digital Sky Survey IV has been provided by the Alfred P. Sloan Foundation, the U.S. Department of Energy Office of Science, and the Participating Institutions. SDSS acknowledges support and resources from the Center for High-Performance Computing at the University of Utah. The SDSS web site is www.sdss.org. SDSS is managed by the Astrophysical Research Consortium for the Participating Institutions of the SDSS Collaboration including the Brazilian Participation Group, the Carnegie Institution for Science, Carnegie Mellon University, the Chilean Participation Group, the French Participation Group, Harvard-Smithsonian Center for Astrophysics, Instituto de Astrofísica de Canarias, The Johns Hopkins University, Kavli Institute for the Physics and Mathematics of the Universe (IPMU) / University of Tokyo, the Korean Participation Group, Lawrence Berkeley National Laboratory, Leibniz Institut für Astrophysik Potsdam (AIP), Max-Planck-Institut für Astronomie (MPIA Heidelberg), Max-Planck-Institut für Astrophysik (MPA Garching), Max-Planck-Institut für Extraterrestrische Physik (MPE), National Astronomical Observatories of China, New Mexico State University, New York University, University of Notre Dame, Observatório Nacional / MCTI, The Ohio State University, Pennsylvania State University, Shanghai Astronomical Observatory, United Kingdom Participation Group, Universidad Nacional Autónoma de México, University of Arizona, University of Colorado Boulder, University of Oxford, University of Portsmouth, University of Utah, University of Virginia, University of Washington, University of Wisconsin, Vanderbilt University, and Yale University.

DATA AVAILABILITY

Data from the IllustrisTNG simulations are publicly available at www.tng-project.org. Data specific to this paper are available on request from the corresponding author.

REFERENCES

Ade P. A. et al., 2016, A&A, 594, A13
Barnes J. E., Hernquist L. E., 1991, ApJ, 370, L65
Barro G. et al., 2017, ApJ, 840, 47
Bell E. F., 2008, ApJ, 682, 355
Bluck A. F. L., Mendel J. T., Ellison S. L., Moreno J., Simard L., Patton D. R., Starkenburg E., 2014, MNRAS, 441, 599
Bournaud F., Dekel A., Teyssier R., Cacciato M., Daddi E., Juneau S., Shankar F., 2011, ApJ, 741, L33
Bundy K. et al., 2015, ApJ, 798, 7
Cattaneo A., Teyssier R., 2007, MNRAS, 376, 1547
Chen Z. et al., 2020, ApJ, 897, 102
Cheung E. et al., 2012, ApJ, 760, 131
Choi E., Somerville R. S., Ostriker J. P., Naab T., Hirschmann M., 2018, ApJ, 866, 91
Cox T. J., Jonsson P., Somerville R. S., Primack J. R., Dekel A., 2008, MNRAS, 384, 386
Damjanov I. et al., 2011, ApJ, 739, L44
Danovich M., Dekel A., Hahn O., Ceverino D., Primack J., 2015, MNRAS, 449, 2087
Dekel A., Burkert A., 2014, MNRAS, 438, 1870
Donnari M. et al., 2019, MNRAS, 485, 4817
Duckworth C., Tojeiro R., Kraljic K., 2020, MNRAS, 492, 1869
Elmegreen B. G., 2011, ApJ, 737, 10
Fall S. M., 1983, IAU Symp., Internal Kinematics and Dynamics of Galaxies, Cambridge University Press. p. 391
Fall S. M., Efstathiou G., 1980, MNRAS, 193, 189
Fang J. J., Faber S. M., Koo D. C., Dekel A., 2013, ApJ, 776, 63
Friedli D., Benz W., 1995, A&A, 301, 649
Garrison-Kimmel S. et al., 2018, MNRAS, 481, 4133
Genel S. et al., 2018, MNRAS, 474, 3976
Gensior J., Kruijssen J. M. D., Keller B. W., 2020, MNRAS, 495, 199
Genzel R., Eisenhauer F., Gillessen S., 2010, Rev. Mod. Phys., 82, 3121
Ghez A. M. et al., 2008, ApJ, 689, 1044
Hopkins P. F., Hernquist L., Cox T. J., Di Matteo T., Robertson B., Springel V., 2006, ApJSS, 163, 1
Hopkins P. F. et al., 2009, MNRAS, 397, 802
Immeli A., Samland M., Gerhard O., Westera P., 2004, A&A, 413, 547
Inoue S., Dekel A., Mandelker N., Ceverino D., Bournaud F., Primack J., 2016, MNRAS, 456, 2052
Kauffmann G., White S. D. M., Heckman T. M., Menard B., Brinchmann J., Charlot S., Tremonti C., Brinkmann J., 2004, MNRAS, 353, 713
Kepner J. V., 1999, ApJ, 520, 59
Lapiner S., Dekel A., Dubois Y., 2020, preprint (arXiv:2012.09186)
Luo Y. et al., 2020, MNRAS, 493, 1686
Marinacci F. et al., 2018, MNRAS, 480, 5113
Martig M., Bournaud F., Teyssier R., Dekel A., 2009, ApJ, 707, 250
Mendel J. T., Simard L., Ellison S. L., Patton D. R., 2013, MNRAS, 429, 2212
Mihos C., Hernquist L., 1996, ApJ, 464, 641
Moreno J., Torrey P., Ellison S. L., Patton D. R., Bluck A. F., Bansal G., Hernquist L., 2015, MNRAS, 448, 1107
Mosleh M., Tacchella S., Renzini A., Marcella Carollo C., Molaeinezhad A., Onodera M., Khosroshahi H. G., Lilly S., 2017, ApJ, 837, 2
Naab T., Johansson P. H., Ostriker J. P., 2009, ApJ, 699, L178
Naiman J. P. et al., 2018, MNRAS, 477, 1206
Nelson E. J. et al., 2012, ApJ, 747, L28
Nelson D. et al., 2018, MNRAS, 475, 624
Nelson D. et al., 2019, Comput. Astrophys. Cosmol., 6, 2
Pérez E. et al., 2013, ApJ, 764, L1
Pillepich A. et al., 2017, MNRAS, 473, 4077
Price-Whelan A. M. et al., 2018, AJ, 156, 18
Robitaille T. P. et al., 2013, A&A, 558, A33
Rodriguez-Gomez V. et al., 2015, MNRAS, 449, 49
Romanowsky A. J., Fall S. M., 2012, ApJSS, 203, 17
Romeo A. B., Wiegert J., 2011, MNRAS, 416, 1191
Roškar R., Debattista V. P., Stinson G. S., Quinn T. R., Kaufmann T., Wadsley J., 2008, ApJ, 675, L65
Sales L. V., Navarro J. F., Theuns T., Schaye J., White S. D. M., Frenk C. S., Crain R. A., Vecchia C. D., 2012, MNRAS, 423, 1544
Saracco P., Gargiulo A., Longhetti M., 2012, MNRAS, 422, 3107
Schawinski K. et al., 2014, MNRAS, 440, 889
Springel V., White S. D., Tormen G., Kauffmann G., 2001, MNRAS, 328, 726
Springel V. et al., 2018, MNRAS, 475, 676
Stewart K. R. et al., 2017, ApJ, 843, 47
Strateva I., Ivezic Z., Knapp G. R., Narayanan V. K., Strauss M. A., 2001, AJ, 122, 1861
Tacchella S. et al., 2015, Science, 348, 314
Tacchella S., Dekel A., Carollo C. M., Ceverino D., DeGraf C., Lapiner S., Mandelker N., Primack J. R., 2016, MNRAS, 457, 2790
Tacchella S., Carollo C. M., Faber S. M., Cibinel A., Dekel A., Koo D. C., Renzini A., Woo J., 2017, ApJ, 844, L1
Tacchella S. et al., 2019, MNRAS, 487, 5416
Teimoorinia H., Bluck A. F. L., Ellison S. L., 2016, MNRAS, 457, 2086
Teklu A. F., Remus R. S., Dolag K., Beck A. M., Burkert A., Schmidt A. S., Schulze F., Steinborn L. K., 2015, ApJ, 812, 29
Terrazas B. A. et al., 2020, MNRAS, 493, 1888
Tissera P. B., Machado R. E. G., Sanchez-Blazquez P., Pedrosa S. E., Sánchez S. F., Snaith O., Vilchez J., 2016, A&A, 592, A93

[2] http://www.astropy.org

Toomre A., 1964, ApJ, 139, 1217
van Dokkum P. G. et al., 2014, ApJ, 791, 45
van den Bosch F. C., 1998, ApJ, 507, 601
van den Bosch F. C., 2001, MNRAS, 331, 98
van der Wel A. et al., 2014, ApJ, 788, 28
Weinberger R. et al., 2017, MNRAS, 465, 3291
Weinberger R. et al., 2018, MNRAS, 479, 4056
Wellons S. et al., 2016, MNRAS, 456, 1030
Woo J., Ellison S. L., 2019, MNRAS, 487, 1927
Woo J., Dekel A., Faber S. M., Koo D. C., 2015, MNRAS, 448, 237
Woo J., Carollo C. M., Faber S. M., Dekel A., Tacchella S., 2017, MNRAS, 464, 1077
Wuyts S. et al., 2011, ApJ, 742, 96
Zavala J. et al., 2016, MNRAS, 460, 4466
Zinger E. et al., 2020, MNRAS, 499, 768
Zolotov A. et al., 2015, MNRAS, 450, 2327

SUPPORTING INFORMATION

Supplementary data are available at *MNRAS* online.

APPENDIX A. Convergence.

Please note: Oxford University Press is not responsible for the content or functionality of any supporting materials supplied by the authors. Any queries (other than missing material) should be directed to the corresponding author for the article.

This paper has been typeset from a TEX/LATEX file prepared by the author.